# Wind load estimation and virtual sensing in long-span suspension bridges using physics-informed Gaussian process latent force models

Petersen, W.; Øiseth, O.; Lourens, E.

**DOI**
10.1016/j.ymssp.2021.108742

**Publication date**
2022

**Document Version**
Final published version

**Published in**
Mechanical Systems and Signal Processing

Mechanical Systems and Signal Processing 170 (2022) 108742

Contents lists available at ScienceDirect

Mechanical Systems and Signal Processing

journal homepage: www.elsevier.com/locate/ymssp

# Wind load estimation and virtual sensing in long-span suspension bridges using physics-informed Gaussian process latent force models

Ø.W. Petersen [a,*], O. Øiseth [a], E. Lourens [b]

[a] NTNU, Norwegian University of Science and Technology, 7491 Trondheim, Norway
[b] TU Delft, 2628 CD Delft, Netherlands

ARTICLE INFO

Communicated by M. Beer

*Keywords:*
Force identification
Virtual sensing
Latent force model
Gaussian process
Structural monitoring
Response prediction
Suspension bridge
Wind engineering

ABSTRACT

Wind loading is an essential aspect in the design and assessment of long-span bridges, but it is often not well-known and cannot be measured directly. Most structural health monitoring systems can easily measure structural responses at discrete locations using accelerometers. This data can be combined with reduced-order modal models in Kalman filter-based algorithms for an inverse estimation of wind loads and system states. As a further development, this work investigates the incorporation of Gaussian process latent force models (GP-LFMs), which can characterize the evolution of the wind loading. The Hardanger Bridge, a 1310 m long suspension bridge instrumented with a monitoring system for wind and vibrations, is used as a case study. It is shown how the LFMs can be enriched with physical information about the stochastic wind loads using monitoring anemometer data and aerodynamic coefficients from wind tunnel tests. It is found that the estimates of the modal wind loads and modal states obtained from a Kalman filter and Rauch–Tung–Striebel smoother are stable for acceleration output only, thus avoiding the accumulation of errors. The proposed approach demonstrates how physical or environmental data can be injected as valuable information for global monitoring strategies and virtual sensing in bridges.

## 1. Introduction

Live loadings on large structures such as bridges, tall buildings, and wind turbines are not always well-known due to their stochastic nature, limited information concerning site-specific conditions, and other uncertainties in the existing load models. Reducing these uncertainties is an important objective in structural health monitoring (SHM)-based infrastructure management [1], as the loads are important inputs in calculations for fatigue, extreme values, and serviceability criteria. Since direct measurements of loads are not viable for large-scale structures in operation, an appealing alternative is indirect force identification by using a limited number of measured structural responses to reconstruct the forces and the states in a dynamic system.

To this end, a number of methods have been proposed. In the past decade, broad attention has been given to different Kalman filter variants for state and input estimation [2–7]. A more recent proposal was the fusion of latent force models (LFMs) [8] into classic force identification, which considers the unknown forces as random Gaussian processes that can be characterized by tunable covariance functions acting as a non-parametric representation of the underlying physics behind the dynamic evolution of the loads. The LFM approach also brings new light to a key challenge in force identification, namely, the instabilities related to filtering based on acceleration output only, for which remedies have also been proposed in other notable works [2,9,10]. The use of LFMs has also

* Corresponding author.
*E-mail addresses:* oyvind.w.petersen@ntnu.no (ØW. Petersen), ole.oiseth@ntnu.no (O. Øiseth), e.lourens@tudelft.nl (E. Lourens).
*URL:* https://www.ntnu.edu/kt/research/dynamics (ØW. Petersen).

https://doi.org/10.1016/j.ymssp.2021.108742
Received 8 April 2021; Received in revised form 21 October 2021; Accepted 8 December 2021
Available online 21 January 2022

been extended to system identification for structures with unknown inputs [11], as well as proposals for bridge response estimation from on-vehicle measurements [12].

In this paper, the focus is placed on the application of LFMs in the estimation of wind loads acting on long-span bridges, where the wind-induced response always persistently remains a critical factor due to the low natural frequencies of such structures. In the field of wind engineering, wind load models used in bridge design are mainly based on theoretical formulas, environmental data, wind tunnel tests, and computational simulations. However, these data sources do not always account for the environmental complexities leading to the actual load conditions on a specific bridge. This can lead to discrepancies between predicted and measured behaviours as noted in several studies [13–20], indicating gaps in the models. Missing environmental data can also be the culprit since dense wind measurements are difficult for very large structures. The wind load inputs are rarely precisely known for real structures, although their effect is observable and typical in the form of dynamic responses due to turbulence or vortex-induced vibrations that can be measured at discrete locations; accelerometers are the most popular option for recording these observations. The numerous uncertainties in wind loading, as well as moving loads in bridges with heavy traffic volume, have led to a high number of monitoring systems being installed on long-span bridges; see, for instance, the reviews in [21–24].

In the present investigation, data collected from the Hardanger Bridge is used [25]. This bridge has been a subject of previous studies on similar topics [26,27]. As a further development, aerodynamic data from wind tunnel tests and environmental data in the form of measured wind velocities from the bridge monitoring system are used to augment the LFMs with information about the stochastic wind loading. The use of LFMs in a force identification context provides a flexible way to impose physics-based temporal or frequency characteristics of the loading such as smoothness or periodicity. In recent terminology, the term physics-informed machine learning has been used to describe the grey-box approach where data-based machine learning algorithms are enriched with physical relations; see, for example, [28]. Finally, the acceleration response measurements are used in a Kalman filter and smoother for identification of the modal wind loads and states.

Section 2 presents classic formulations for wind loading on bridges and then introduces the LFM theory. Section 3 presents the case study, going through the steps of wind field analysis, generating the LFM for the wind loads, and finally performing the state and load estimation. Conclusions are given in Section 4.

## 2. Theoretical background

### 2.1. Classic modelling of static and buffeting wind loads on bridge decks

This section presents the main equations for the wind loading on bridges by assuming linearized theory for the wind-induced buffeting response (i.e. dynamics due to turbulent wind), which we will refer to as the classic wind model (CWM). For a more comprehensive background on modelling of wind loads on structures, the reader is referred to books on this subject [29–31]. The linear equation of motion for the response $\mathbf{r}(t)$ reads as follows:

$$\mathbf{M}_0\ddot{\mathbf{r}}(t) + (\mathbf{C}_0 - \mathbf{C}_{\mathrm{ae}})\dot{\mathbf{r}}(t) + (\mathbf{K}_0 - \mathbf{K}_{\mathrm{ae}})\mathbf{r}(t) = \mathbf{f}_{\mathrm{b}}(t) \tag{1}$$

where subscripts 0 and *ae* respectively denote contributions from still-air structural properties and aeroelastic properties. The subscript *b* for the load vector denote buffeting (fluctuating) forces. The self-excited forces are taken into account by the stiffness and damping matrices $\mathbf{K}_{\mathrm{ae}}$ and $\mathbf{C}_{\mathrm{ae}}$, which are assumed to be constant for a time window with stationary wind conditions. For bridges mainly loaded by wind actions, the response is dominated by low-frequent vibrations. In the model order reduction $\mathbf{r}(t) \approx \boldsymbol{\Phi}\mathbf{z}(t)$, a selected set of $\mathrm{n_m}$ still-air vibration modes (solved from the still-air undamped eigenvalue problem considering $\mathbf{M}_0$ and $\mathbf{K}_0$) are used as generalized shape functions. The generalized equation of motion then reads:

$$\tilde{\mathbf{M}}_0\ddot{\mathbf{z}}(t) + (\tilde{\mathbf{C}}_0 - \tilde{\mathbf{C}}_{\mathrm{ae}})\dot{\mathbf{z}}(t) + (\tilde{\mathbf{K}}_0 - \tilde{\mathbf{K}}_{\mathrm{ae}})\mathbf{z}(t) = \boldsymbol{\Phi}^{\mathrm{T}}\mathbf{f}_{\mathrm{b}}(t) \tag{2}$$

where the notation $\tilde{(\cdot)}$ denotes the generalized system matrices. By introducing the modal state vector $\mathbf{x}(t) = [\mathbf{z}(t)^{\mathrm{T}} \;\; \dot{\mathbf{z}}(t)^{\mathrm{T}}]^{\mathrm{T}}$, the equation above can be reformulated in state-space form as follows:

$$\dot{\mathbf{x}}(t) = \mathbf{A}_{\mathrm{c}}\mathbf{x}(t) + \mathbf{B}_{\mathrm{c}}\mathbf{p}(t) \tag{3}$$

$$\mathbf{A}_{\mathrm{c}} = \begin{bmatrix} \mathbf{0} & \mathbf{I} \\ -\tilde{\mathbf{M}}_0^{-1}(\tilde{\mathbf{K}}_0 - \tilde{\mathbf{K}}_{\mathrm{ae}}) & -\tilde{\mathbf{M}}_0^{-1}(\tilde{\mathbf{C}}_0 - \tilde{\mathbf{C}}_{\mathrm{ae}}) \end{bmatrix}, \quad \mathbf{B}_{\mathrm{c}} = \begin{bmatrix} \mathbf{0} \\ \tilde{\mathbf{M}}_0^{-1} \end{bmatrix} \tag{4}$$

where $\mathbf{p}(t) = \boldsymbol{\Phi}^{\mathrm{T}}\mathbf{f}_{\mathrm{b}}(t)$ are designated as the modal buffeting loads. To ease verification, the effective modal properties are given by the eigenvalue problem:

$$\left[\mathbf{A}_{\mathrm{c}} - \lambda_j\mathbf{I}\right]\begin{bmatrix} \boldsymbol{\psi}_j \\ \boldsymbol{\psi}_j\lambda_j \end{bmatrix} = \mathbf{0} \quad \text{and} \quad \left[\mathbf{A}_{\mathrm{c}} - \lambda_j^*\mathbf{I}\right]\begin{bmatrix} \boldsymbol{\psi}_j^* \\ \boldsymbol{\psi}_j^*\lambda_j^* \end{bmatrix} = \mathbf{0} \tag{5}$$

where the eigenvalues have the complex conjugate form $\lambda_j, \lambda_j^* = -\xi_j\omega_j \pm i\omega_j\sqrt{1-\xi_j^2}$, so that the undamped natural frequency (in rad/s) is $\omega_j = |\lambda_j|$ and the critical damping ratio is $\xi_j = -\mathrm{Real}(\lambda_j)/|\lambda_j|$. $\boldsymbol{\psi}_j$ alters the still-air mode shapes $\boldsymbol{\Phi}$ so that the in-wind modes are given by $[\boldsymbol{\psi}_1, \ldots, \boldsymbol{\psi}_{\mathrm{n_m}}]\boldsymbol{\Phi}$.

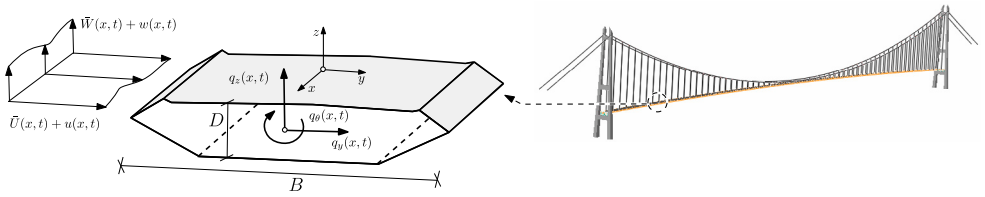


**Fig. 1.** Wind velocity field and resulting buffeting loads acting on the bridge deck.

Next, the classic theory for the modelling of wind loads due to turbulence is considered. In accordance with Fig. 1 the distributed buffeting forces acting on the bridge deck are given by [30]:

$$\begin{bmatrix} q_{\mathrm{b},y}(x,t) \\ q_{\mathrm{b},z}(x,t) \\ q_{\mathrm{b},\theta}(x,t) \end{bmatrix} = \frac{1}{2}\rho\bar{U}(x,t)B \begin{bmatrix} 2(D/B)\bar{C}_D & (D/B)C'_D - \bar{C}_L \\ 2\bar{C}_L & C'_L + (D/B)\bar{C}_D \\ 2B\bar{C}_M & BC'_M \end{bmatrix} \begin{bmatrix} u(x,t) \\ w(x,t) \end{bmatrix} \tag{6}$$

or written compactly as:

$$\mathbf{q}_{\mathrm{b}}(x,t) = \mathbf{B}_{\mathbf{q}}(x)\mathbf{v}(x,t) \tag{7}$$

where $u(x,t)$ and $w(x,t)$ are the alongwind and vertical turbulence components. Furthermore, $\rho$ is the air density, $\bar{U}(x,t)$ is the mean alongwind velocity, $\bar{W}(x,t)$ is the vertical velocity, and $D$ and $B$ are the height and width of the bridge deck. $\{\bar{C}_D, \bar{C}_L, \bar{C}_M\}$ and $\{C'_D, C'_L, C'_M\}$ are the linearized mean and slope of coefficients for drag, lift and pitching moment, which are commonly obtained in wind tunnel experiments using scale section models or sometimes using computational fluid dynamics. Aerodynamic admittance (transfer functions relating surface pressures to wind forces) have been omitted from Eq. (6) due to a lack of data, but this phenomenon effectively acts as a low-pass filter [32].

In the stochastic characterization of a wind field, a two-point statistical description of the wind velocity is commonly expressed using a cross-spectral density format as follows:

$$\mathbf{S}_{\mathbf{vv}}(\omega, x_1, x_2) = \begin{bmatrix} S_{uu}(\omega, x_1, x_2) & S_{uw}(\omega, x_1, x_2) \\ S_{wu}(\omega, x_1, x_2) & S_{ww}(\omega, x_1, x_2) \end{bmatrix} = \begin{bmatrix} \sqrt{S_u(\omega, x_1)S_u(\omega, x_2)}C_{uu}(\omega, \Delta x) & \sqrt{S_u(\omega, x_1)S_w(\omega, x_2)}C_{uw}(\omega, \Delta x) \\ \sqrt{S_u(\omega, x_2)S_w(\omega, x_1)}C_{uw}(\omega, \Delta x) & \sqrt{S_w(\omega, x_1)S_w(\omega, x_2)}C_{ww}(\omega, \Delta x) \end{bmatrix} \tag{8}$$

where $\Delta x = |x_1 - x_2|$ is the span-wise distance between the two points. $S_u(\omega)$ and $S_w(\omega)$ are single-point spectral densities. $C_{uu}(\omega, \Delta x)$ and $C_{ww}(\omega, \Delta x)$ are root-coherence functions for which the commonly applied Davenport model reads [33]:

$$C_{mm}(\omega, \Delta x) = \exp\left(-K_m \frac{\omega\, \Delta x}{2\pi\bar{U}}\right), \quad m \in \{u, w\} \tag{9}$$

which relies on given decay coefficients $K_u$ and $K_w$. This expression has the critiqued shortcoming of assuming a value close to unity for frequencies close to zero, even for large spatial separations, which is not physical. However, this approach remains heavily used due to its simplicity and lack of proper alternatives, except for a few more sophisticated models that have been proposed [34]. We also assume $C_{uw}(\omega, \Delta x) = 0$, i.e., no significant correlation among $u(x,t)$ and $w(x,t)$.

By integrating the buffeting forces along the whole span, the spectral density matrix for modal buffeting loads can then be calculated by:

$$\mathbf{S}_{\mathbf{pp}}(\omega) = \int_0^L \int_0^L \mathbf{\Phi}_{\mathrm{ae}}(x_1)^{\mathrm{T}} \mathbf{B}_{\mathbf{q}}(x_1)\, \mathbf{S}_{\mathbf{vv}}(\omega, x_1, x_2)\, \mathbf{B}_{\mathbf{q}}(x_2)^{\mathrm{T}}\, \mathbf{\Phi}_{\mathrm{ae}}(x_2)\, \mathrm{d}x_1\, \mathrm{d}x_2 \tag{10}$$

where $\mathbf{\Phi}_{\mathrm{ae}}(x)$ is a matrix containing the modal values in the lateral ($y$), vertical ($z$), and pitching ($\theta$) degrees of freedom (DOFs) of the box girder:

$$\mathbf{\Phi}_{\mathrm{ae}}(x) = \begin{bmatrix} \phi_y^{(1)}(x) & \dots & \phi_y^{(\mathrm{n_m})}(x) \\ \phi_z^{(1)}(x) & \dots & \phi_z^{(\mathrm{n_m})}(x) \\ \phi_\theta^{(1)}(x) & \dots & \phi_\theta^{(\mathrm{n_m})}(x) \end{bmatrix}, \quad x \in [0, L] \tag{11}$$

The cross-covariance matrix, which will be used later, is calculated by the inverse Fourier transform:

$$\boldsymbol{\kappa}_{\mathbf{pp}}(\tau) = \int_{-\infty}^{\infty} \mathbf{S}_{\mathbf{pp}}(\omega) \exp(i\omega\tau)\, \mathrm{d}\omega \tag{12}$$

Although the loading on the cables is small in comparison, the linearized distributed drag load on the main cables can be expressed as:

$$q_{\mathrm{b},cable,y}(x,t) = \rho\bar{U}(x,t)H_{cable}C_{D,cable}u(x,t) \tag{13}$$

where $H_{cable}$ is the diameter and $C_{D,cable}$ is a cylindrical drag coefficient. Similarly, these forces can be transformed to the modal domain and added to the spectral density for the modal load.

In classic wind engineering analysis for bridges, a quantification of the bridge response is usually the objective. When the spectral density of the load is available (Eq. (10)), the stochastic description of the modal dynamic response is also straightforward:

$$\mathbf{S}_{\mathbf{zz}}(\omega) = \tilde{\mathbf{H}}_{\mathbf{pz}}(\omega)\mathbf{S}_{\mathbf{pp}}(\omega)\tilde{\mathbf{H}}_{\mathbf{pz}}^{\mathrm{H}}(\omega) \tag{14}$$

where the transfer function of the modal system in Eq. (2) is defined as:

$$\tilde{\mathbf{H}}_{\mathbf{pz}}(\omega) = [-\omega^2\tilde{\mathbf{M}}_0 + i\omega(\tilde{\mathbf{C}}_0 - \tilde{\mathbf{C}}_{\mathrm{ae}}) + (\tilde{\mathbf{K}}_0 - \tilde{\mathbf{K}}_{\mathrm{ae}})]^{-1} \tag{15}$$

This can promptly be transformed back to the spectral densities of displacement or acceleration responses:

$$\mathbf{S}_{\mathbf{rr}}(\omega) = \mathbf{\Phi}\mathbf{S}_{\mathbf{zz}}(\omega)\mathbf{\Phi}^{\mathrm{T}}, \quad \mathbf{S}_{\ddot{\mathbf{r}}\ddot{\mathbf{r}}}(\omega) = \omega^4\mathbf{S}_{\mathbf{rr}}(\omega) \tag{16}$$

The methodology in this section is based on assumed models for the stochastic wind loads. Although these models are widely applied, it is also accepted that they rarely result in perfect predictions of the dynamic response [19,35]. In the next section, a framework for inverse identification of the wind loads is introduced.

### 2.2. Gaussian process latent force model

Gaussian process (GP) regression is a powerful tool in the analysis of distributed data such as time series [36], and it briefly presented in the following. Let $f(t)$ be a GP prior with mean $\mu(t)$ and covariance function $\kappa(t,t')$. Next, it is assumed we have $N$ noisy observations $y(t_k) = f(t_k) + \upsilon_k$ available at time instants $\mathbf{t} = \{t_1, t_2, \dots, t_N\}$, which are collected in the vector $\mathbf{y} = [y(t_1), \dots, y(t_N)]^{\mathrm{T}}$, where $\mathbb{E}[\upsilon_k^2] = \sigma_n^2$ is the variance of the Gaussian noise. The GP regression deals with the problem of inferring the function value $f(t_*)$ for the new point $t_*$. Conditioned on the observed data, it can be shown that the posterior distribution for $f(t_*)$ also is Gaussian with the following mean and covariance:

$$\mathbb{E}[f(t_*) \mid \mathbf{y}] = \boldsymbol{\kappa}(t_*, \mathbf{t})\big(\boldsymbol{\kappa}(\mathbf{t},\mathbf{t}) + \sigma_n^2\mathbf{I}\big)^{-1}\big(\mathbf{y} - \boldsymbol{\mu}(\mathbf{t})\big) + \mu(t_*) \tag{17}$$

$$\mathrm{Cov}[f(t_*) \mid \mathbf{y}] = \kappa(t_*, t_*) - \boldsymbol{\kappa}(t_*, \mathbf{t})\big(\boldsymbol{\kappa}(\mathbf{t},\mathbf{t}) + \sigma_n^2\mathbf{I}\big)^{-1}\boldsymbol{\kappa}(t_*, \mathbf{t})^{\mathrm{T}} \tag{18}$$

Further details can be found in [37]. Whereas the classic GP regression suffers from scaling problems since it eventually involves inverting very large matrices (proportional to the number of training data points), the discrete state-space formulation of the GP-LFM discussed in the following has the benefit of a first-order Markov property (i.e., compact recursive formulations). This allows very long time series to be processed without problems related to the scale of the data set.

In the context of this paper, the GP-LFM represents the stochastic evolution of the excitation forces on the structure. In this work, to design the LFM, we assume the wind loading is stationary for a 10-min time window, meaning that the GPs can be characterized by first- and second-order statistical moments, i.e. a mean value usually equal to zero and a stationary covariance function. The wind loads are treated as a realization of a white noise GP denoted $\tilde{w}(t)$ with variance $\sigma_{\tilde{w}}^2 = \mathbb{E}[\tilde{w}(t)^2]$ that is filtered through a designed kernel (not to be confused with the vertical turbulence $w(x,t)$). In the presented application, we have found the Matérn kernel suitable. This is a common class of flexible functions that can effectively regulate smoothness. Specifically, we use the one-half Matérn kernel, meaning each modal force $p_j(t)\,(j = 1, \dots, \mathrm{n_m})$ is treated as the output of a first-order stochastic differential equation:

$$\dot{s}_j(t) = -\lambda_j s_j(t) + \tilde{w}_j(t) \tag{19}$$

$$p_j(t) = s_j(t) \tag{20}$$

In the multivariate case where multiple modal loads are present, it is easiest to consider each of the components independently by constructing the LFM as a block-diagonal system in the following continuous state-space format [8,38]:

$$\begin{bmatrix} \dot{s}_1(t) \\ \vdots \\ \dot{s}_{\mathrm{n_m}}(t) \end{bmatrix} = \begin{bmatrix} F_{\mathrm{c},1} & & \\ & \ddots & \\ & & F_{\mathrm{c},\mathrm{n_m}} \end{bmatrix}\begin{bmatrix} s_1(t) \\ \vdots \\ s_{\mathrm{n_m}}(t) \end{bmatrix} + \begin{bmatrix} L_{\mathrm{c},1} & & \\ & \ddots & \\ & & L_{\mathrm{c},\mathrm{n_m}} \end{bmatrix}\begin{bmatrix} \tilde{w}_1(t) \\ \vdots \\ \tilde{w}_{\mathrm{n_m}}(t) \end{bmatrix} \tag{21}$$

$$\begin{bmatrix} p_1(t) \\ \vdots \\ p_{\mathrm{n_m}}(t) \end{bmatrix} = \begin{bmatrix} H_{\mathrm{c},1} & & \\ & \ddots & \\ & & H_{\mathrm{c},\mathrm{n_m}} \end{bmatrix}\begin{bmatrix} s_1(t) \\ \vdots \\ s_{\mathrm{n_m}}(t) \end{bmatrix} \tag{22}$$

where $F_{\mathrm{c},j} = -\lambda_j$, $L_{\mathrm{c},j} = 1$, $H_{\mathrm{c},j} = 1$, and the subscript $c$ denotes system matrices in continuous time. In compact notation, the LFM is defined as:

$$\dot{\mathbf{s}}(t) = \mathbf{F}_{\mathrm{c}}\mathbf{s}(t) + \mathbf{L}_{\mathrm{c}}\tilde{\mathbf{w}}(t) \tag{23}$$

$$\mathbf{p}(t) = \mathbf{H}_{\mathrm{c}}\mathbf{s}(t) \tag{24}$$

Casting GPs into a state-space form is particularly useful, as this allows the LFM to be incorporated into a Kalman filtering framework [39], which can also be coupled with mechanical state-space models. In general, the matrices $\mathbf{F}_{\mathrm{c}}$, $\mathbf{L}_{\mathrm{c}}$, and $\mathbf{H}_{\mathrm{c}}$ can be

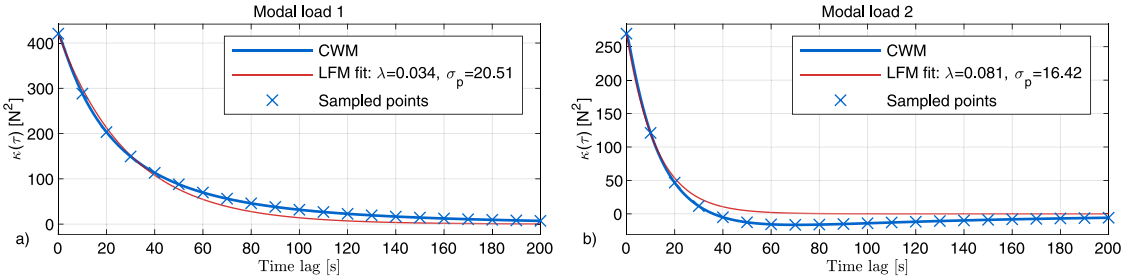


**Fig. 2.** Example of LFM approximation of the wind load.

parameterized through a wide range of available kernel types [8], which can be tailored to the specific problem to control the characteristics of the force, such as periodicity and smoothness. For structural engineering problems, it can be meaningful to consider both the temporal and frequency properties of the LFM. Eqs. (19) and (20) lead to a (two-sided) force spectral density on the form:

$$S_{p,j}(\omega) = \frac{\sigma^2_{\tilde{w},j}}{2\pi(\lambda_j^2 + \omega^2)} \tag{25}$$

The equivalent time-domain representation is the following covariance function:

$$\kappa_{p,j}(\tau) = \mathbb{E}[p_j(t)p_j(t+\tau)] = \frac{\sigma^2_{\tilde{w},j}}{2\lambda_j}\exp(-\lambda_j|\tau|) = \sigma^2_{p,j}\exp(-\lambda_j|\tau|) \tag{26}$$

which is also known as the Ornstein–Uhlenbeck kernel. In the last step, the hyperparameters are re-parameterized slightly by instead using the set $\boldsymbol{\theta}_j = \{\lambda_j, \sigma_{p,j}\} > 0$ for each modal load, where we introduce the variable $\sigma^2_{p,j} = \sigma^2_{\tilde{w},j}/(2\lambda_j)$. In addition to the magnitude factor $\sigma_{p,j}$, it is apparent that the hyperparameter $\lambda_j$ serves the role of inverse length scale in the covariance function Eq. (26). This model can be reasonable for wind engineering problems relating to atmospheric turbulence where the wind loads typically have a slowly decaying covariance function.

Next, the question of properly selecting the values of the LFM hyperparameters arises. In GP regression, the hyperparameters are usually selected from a training data set, using for instance maximum likelihood methods and sometimes cross-validation [37]. One other possibility explored here is utilizing the CWM described in Section 2.1, which here is deemed the best qualified guess for a stochastic characterization of the load.

As an illustration, consider Fig. 2 which shows realistic examples of covariance functions of two wind loads as predicted by the CWM in Section 2.1 for a given set of stationary wind velocity conditions. The figure also shows exponential covariance functions from Eq. (26). The actual selection of the hyperparameter values is based on fitting of equivalent autoregressive models of order 1 (see equations shown in Appendix B). The magnitude and decay behaviour of the covariance functions can be approximated well, but the figure also shows that small compromises are made: for instance, the exponential covariance function in the LFM cannot model the slight negative values in Fig. 2(b). Nevertheless, it is possible to use very simple LFMs to assign a realistic prior belief on the load characteristics. In this context, the wind load prediction from the CWM thus serves as a nominal basis for the expected load. Note that a new set of hyperparameters are obtained for each 10-min period in which the wind loading is assumed to be stationary.

The concept could also be extended to other types of natural loads encountered for structures. For more cyclic or quasi-periodic excitation such as vortex-induced wind forces on cables, narrow-banded wave loading on marine structures, or rotating machinery in wind turbines, it can be expected that kernels with periodicity features [40–42] or sparsity in the frequency domain would be suitable in load identification problems. However, it is necessary that the kernel admits a state-space representation, or can be approximated as such [43,44], in order to seamlessly fuse the LFM with the system response equations as shown later. For the bridge under consideration in this paper, global vortex-induced vibrations are not a particular issue, and this work mainly deals with wind buffeting forces due to turbulence, so the LFM in Eqs. (19)–(20) is deemed sufficient to model the wind load in the identification.

To complete the equations for LFM in matrix form, expressions for autocovariance functions and spectral densities can be found. For the matrix system in Eqs. (23)–(24), it can be shown that the vector $\mathbf{p}(t)$ is a GP with cross-covariance matrix $\boldsymbol{\kappa}_{\mathbf{pp}}(\tau)$, which can be calculated as follows [8]:

$$\boldsymbol{\kappa}_{\mathbf{pp}}(\tau) = \mathbf{H}_c\mathbf{P}_c^{\infty}\exp(\mathbf{F}_c\tau)^{\mathrm{T}}\mathbf{H}_c^{\mathrm{T}} \quad , \quad \tau \geq 0 \tag{27}$$

The matrix $\mathbf{P}_c^{\infty}$ is solved from the state-steady condition of Eqs. (23) and (24) by the algebraic Ricatti equation:

$$\mathbf{F}_c\mathbf{P}_c^{\infty} + \mathbf{P}_c^{\infty}\mathbf{F}_c^{\mathrm{T}} + \mathbf{L}_c\mathbf{Q}_{\tilde{w}c}\mathbf{L}_c^{\mathrm{T}} = \mathbf{0} \tag{28}$$

where $\mathbf{Q}_{\tilde{w}c}$ is a diagonal covariance matrix populated with the variances $\sigma^2_{\tilde{w},j}$. Alternatively, the cross-covariance matrix can be calculated via the inverse Fourier transform as $\boldsymbol{\kappa}_{\mathbf{pp}}(\tau) = \int_{-\infty}^{\infty} \mathbf{S}_{\mathbf{pp}}(\omega) \exp(i\omega\tau)\, \mathrm{d}\omega$, where the spectral density of the latent forces is given by:

$$\mathbf{S}_{\mathbf{pp}}(\omega) = \mathbf{H}_{\tilde{\mathbf{w}}\mathbf{p}}(\omega)\mathbf{S}_{\tilde{\mathbf{w}}\tilde{\mathbf{w}}}(\omega)\mathbf{H}^{\mathrm{H}}_{\tilde{\mathbf{w}}\mathbf{p}}(\omega) \tag{29}$$

$$\mathbf{H}_{\tilde{\mathbf{w}}\mathbf{p}}(\omega) = [\mathbf{H}_c(-\mathbf{F}_c + i\omega\mathbf{I})^{-1}\mathbf{L}_c] \tag{30}$$

Here, $\mathbf{S}_{\tilde{\mathbf{w}}\tilde{\mathbf{w}}}(\omega)$ is a diagonal matrix populated with $\sigma^2_{\tilde{w},j}/(2\pi)$. Since the LFM in Eqs. (21)–(22) is a diagonal system, $\boldsymbol{\kappa}_{\mathbf{pp}}(\tau)$ and $\mathbf{S}_{\mathbf{pp}}(\omega)$ will be diagonal matrices with uncoupled elements that can be directly calculated from Eqs. (25)–(26).

Pursuing the option of physics-designed LFMs naturally demands that proper wind field models and aerodynamic coefficients are available for the CWM, or at least that reasonable engineering assumptions are used where specific data are missing. In cases where no specific information on hyperparameters is viable, it is also possible to tune these via optimization of maximum likelihood to the measured output data, which is explained in Section 3.4.

Finally, we believe it can also be argued that, although they represent the same quantity, a methodological distinction should be made between the loading according to the CWM theory (Section 2.1) and the load characterization in the LFM (Section 2.2). The former can be considered a direct modelling approach based on environmental and aerodynamic data with idealized load assumptions such as homogeneity, stationarity, and linearity. The LFM can be seen as a tool for including prior knowledge of the forces in an inverse identification context or learning from real-life data.

### 2.3. Augmented system formulation

Following [8] and reproduced here for completeness, the augmented format is obtained by combining the linear dynamic system in Eq. (3) and the LFM in Eqs. (23) and (24):

$$\begin{bmatrix}\dot{\mathbf{x}}(t)\\ \dot{\mathbf{s}}(t)\end{bmatrix} = \begin{bmatrix}\mathbf{A}_c & \mathbf{B}_c\mathbf{H}_c\\ \mathbf{0} & \mathbf{F}_c\end{bmatrix}\begin{bmatrix}\mathbf{x}(t)\\ \mathbf{s}(t)\end{bmatrix} + \begin{bmatrix}\mathbf{0}\\ \mathbf{L}_c\tilde{\mathbf{w}}(t)\end{bmatrix} \tag{31}$$

or simply:

$$\dot{\mathbf{x}}^{\mathrm{a}}_c(t) = \mathbf{F}_{\mathrm{ac}}\mathbf{x}^{\mathrm{a}}_c(t) + \tilde{\mathbf{w}}^{\mathrm{a}}_c(t) \tag{32}$$

The response measurements $\mathbf{y}(t)$, which can be accelerations or displacements, are assembled as follows:

$$\mathbf{y}(t) = \mathbf{S}_{\mathrm{acc}}\ddot{\mathbf{r}}(t) + \mathbf{S}_{\mathrm{disp}}\mathbf{r}(t) \tag{33}$$

or converted to the state-space format:

$$\mathbf{y}(t) = \mathbf{G}_c\mathbf{x}(t) + \mathbf{J}_c\mathbf{p}(t) = \begin{bmatrix}\mathbf{G}_c & \mathbf{J}_c\mathbf{H}_c\end{bmatrix}\begin{bmatrix}\mathbf{x}(t)\\ \mathbf{s}(t)\end{bmatrix} = \mathbf{H}_{\mathrm{ac}}\mathbf{x}^{\mathrm{a}}_c(t) \tag{34}$$

where the following matrices are defined:

$$\mathbf{G}_c = \begin{bmatrix}\mathbf{S}_{\mathrm{disp}}\boldsymbol{\Phi} - \mathbf{S}_{\mathrm{acc}}\boldsymbol{\Phi}\tilde{\mathbf{M}}_0^{-1}(\tilde{\mathbf{K}}_0 - \tilde{\mathbf{K}}_{\mathrm{ae}}) & -\mathbf{S}_{\mathrm{acc}}\boldsymbol{\Phi}\tilde{\mathbf{M}}_0^{-1}(\tilde{\mathbf{C}}_0 - \tilde{\mathbf{C}}_{\mathrm{ae}})\end{bmatrix} \tag{35}$$

$$\mathbf{J}_c = \begin{bmatrix}\mathbf{S}_{\mathrm{acc}}\boldsymbol{\Phi}\end{bmatrix} \tag{36}$$

Finally, following the standard time-discretization scheme ($t_k = k\Delta t$) in [8] and adding stochastic noise to both the state and output equation, Eqs. (31) and (34) now read as follows:

$$\mathbf{x}^{\mathrm{a}}_{k+1} = \mathbf{F}_{\mathrm{ad}}\mathbf{x}^{\mathrm{a}}_k + \mathbf{w}^{\mathrm{a}}_k, \quad \mathbf{x}^{\mathrm{a}}_k = [\mathbf{x}(t_k)^{\mathrm{T}}\ \mathbf{s}(t_k)^{\mathrm{T}}]^{\mathrm{T}} \tag{37}$$

$$\mathbf{y}_k = \mathbf{H}_{\mathrm{ad}}\mathbf{x}^{\mathrm{a}}_k + \mathbf{v}_k \tag{38}$$

Here, the subscript $d$ denotes system matrices in discrete time, and the system matrices are:

$$\mathbf{F}_{\mathrm{ad}} = \exp(\mathbf{F}_{\mathrm{ac}}\Delta t), \quad \mathbf{H}_{\mathrm{ad}} = \mathbf{H}_{\mathrm{ac}} \tag{39}$$

The covariances of the noise processes are given as follows:

$$\mathbb{E}[\mathbf{v}_k\mathbf{v}_k^{\mathrm{T}}] = \mathbf{R} \tag{40}$$

The covariance of the augmented process noise ($\mathbf{Q}_{\mathrm{ad}} = \mathbb{E}[\mathbf{w}^{\mathrm{a}}_k\mathbf{w}^{\mathrm{a}}_k]$) consists of an integration term relating to the LFM and an added term $\mathbf{Q}_{\mathrm{xd}}$ that accounts for unmodelled dynamics or other noise:

$$\mathbf{Q}_{\mathrm{ad}} = \int_0^{\Delta t} \exp\big(\mathbf{F}_{\mathrm{ac}}(\Delta t - \tau)\big)\mathbf{Q}_{\mathrm{ac}}\exp\big(\mathbf{F}_{\mathrm{ac}}(\Delta t - \tau)^{\mathrm{T}}\big)\,\mathrm{d}\tau + \begin{bmatrix}\mathbf{Q}_{\mathrm{xd}} & \mathbf{0}\\ \mathbf{0} & \mathbf{0}\end{bmatrix} \tag{41}$$

**Fig. 3.** The Hardanger Bridge (Photo: Aksel Fenerci/NTNU).

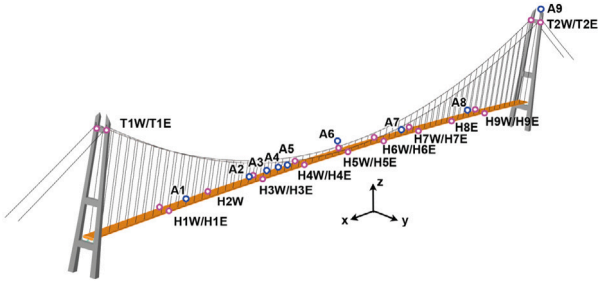


**Fig. 4.** Position of sensors on the bridge: accelerometers (denoted H/T) and anemometers (denoted A).

where we define:

$$\mathbf{Q}_{\mathrm{ac}} = \begin{bmatrix} \mathbf{0} & \mathbf{0} \\ \mathbf{0} & \mathbf{L}_{\mathrm{c}}\mathbf{Q}_{\tilde{w}\mathrm{c}}\mathbf{L}_{\mathrm{c}}^{\mathrm{T}} \end{bmatrix} \tag{42}$$

This state-space model is used in a classic Kalman filter (KF) [45] and subsequently a backward Rauch–Tung–Striebel (RTS) smoother [46] to estimate the augmented state vector $\hat{\mathbf{x}}_k^{\mathrm{a}}$ (see equations in Appendix A), from which the modal state estimate $\hat{\mathbf{z}}(t)$ and modal load estimate $\hat{\mathbf{p}}(t) = \mathbf{H}_{\mathrm{c}}\hat{\mathbf{s}}(t)$ are available.

## 3. Utilizing environmental and acceleration data for identification of modal loads and responses

### 3.1. Monitoring data from the Hardanger Bridge

The Hardanger Bridge (Fig. 3) is a long-span suspension bridge ($L = 1310$ m). This structure has been monitored since 2013 to study both the wind conditions and wind-induced dynamic responses, which are highly important for bridges of such scales. In the monitoring campaign, accelerations from 20 triaxial accelerometers and wind velocities from 9 sonic anemometers were recorded. Fig. 4 shows the positions of the sensors, and details about the instrumentation setup can be found in [25,47]. The monitoring data from this bridge is also made available, and we refer to [25] for details on accessing the data repository.

In this application, a time series that is 3.5 h long is chosen. The measurement data is resampled down to a rate of 20 Hz ($\Delta t = 0.05$ s). The time series is divided into 10-min intervals for which all steps in the analysis are performed. In the following sections, the analysis and processing steps of the different data are explained. The crafting of the models and the different data sources is summarized in Fig. 5.

### 3.2. Analysis of wind data

The wind measurements at the mid-span of the bride are shown in Fig. 6. The statistics for the mean wind velocities ($\bar{U}, \bar{W}$) for 10-min intervals and turbulence intensities ($I_u = \sigma_u/\bar{U}, I_w = \sigma_w/\bar{U}$) from anemometer A2–A8 are shown in Fig. 7 (data from anemometer A1 was not available). As a general trend, both the mean wind velocity and the turbulence are greater in the last half of this time series, which can be expected to also influence the bridge response accordingly. For the location of the bridge, a Kaimal-type (one-sided) spectrum [48] has been shown to adequately model the single-point statistics of the wind turbulence [47]:

$$\frac{S_m(f)f}{\sigma_m^2} = \frac{A_m f_z}{(1 + 1.5A_m f_z)^{5/3}}, \quad f_z = \frac{fz}{\bar{U}}, \quad m \in \{u, w\} \tag{43}$$

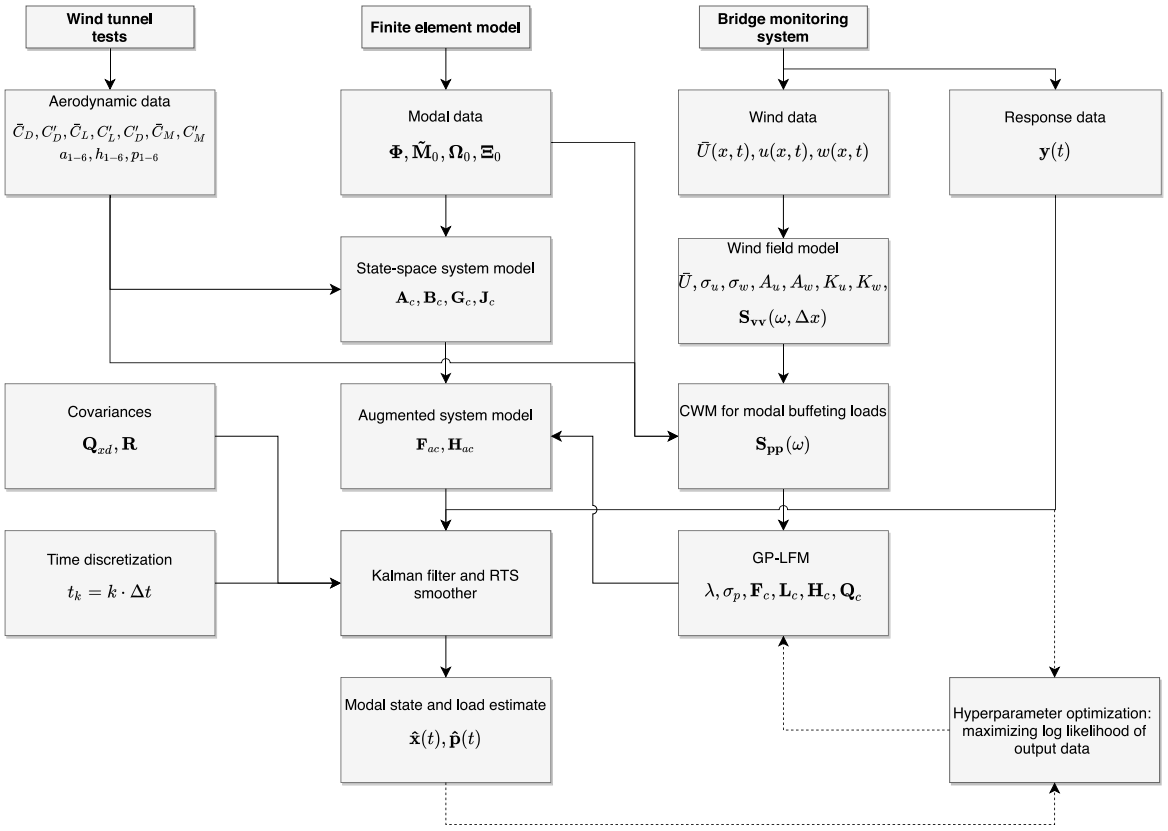


**Fig. 5.** Main steps in the processing of the models and data leading to the load and state estimates.

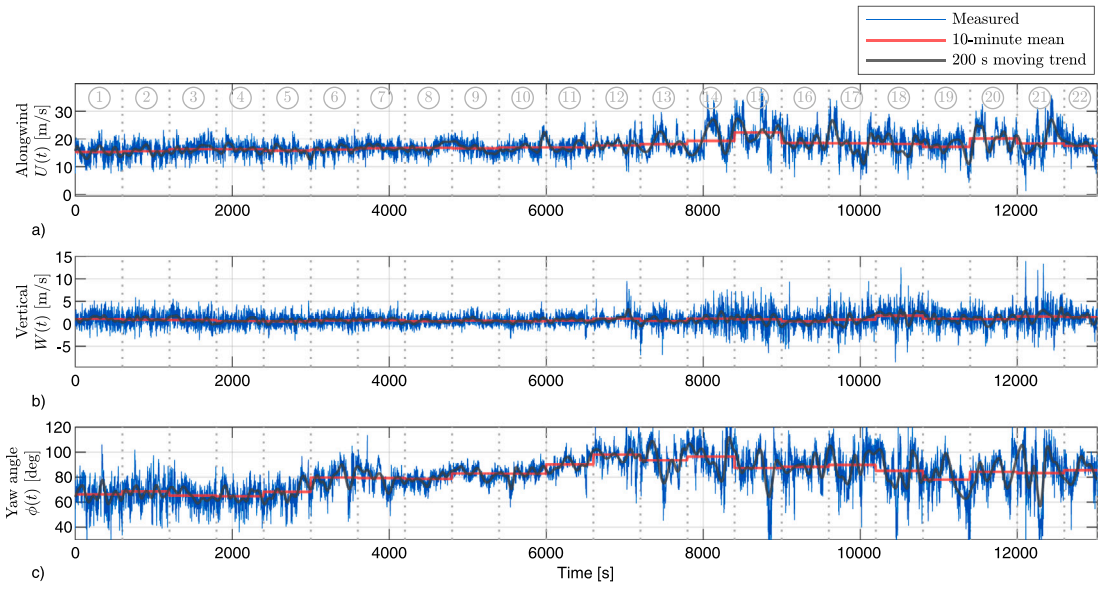


**Fig. 6.** Measured with velocities at the anemometer in the mid-span of the bridge. The circled numbers and dashed vertical lines indicate the 10-min period windows.

Here, $z = 60$ m is the bridge deck elevation above the water. For each of the anemometers A2–A8, the spectral density of the turbulence $u(t)$ and $w(t)$ is calculated from the Welch method (using Hamming windows with a length of 120 s and 50% overlap),

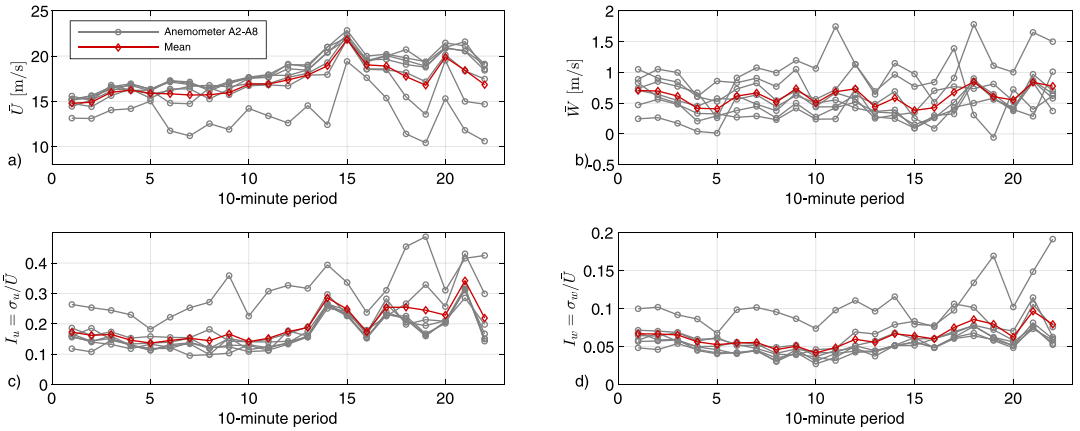


**Fig. 7.** Wind statistics from anemometer A2–A8: (a) mean alongwind velocity; (b) mean vertical wind velocity; (c) alongwind turbulence intensity; (d) vertical turbulence intensity.

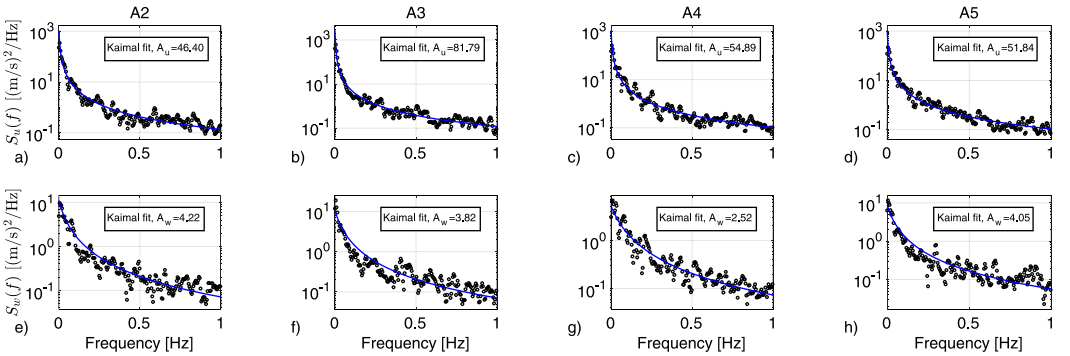


**Fig. 8.** Fit of Kaimal spectrum of wind turbulence for a typical 10-min period shown for anemometers A2–A5: (a–d): alongwind turbulence; (e–h): vertical turbulence.

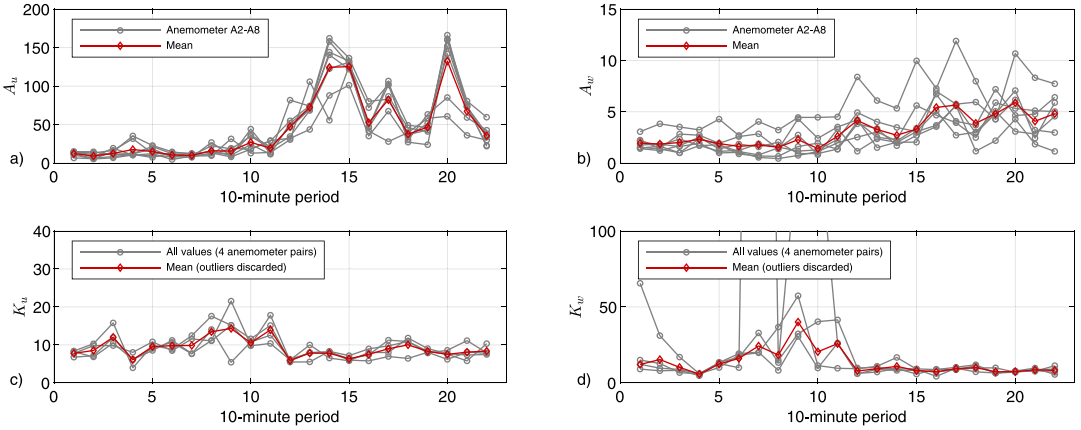


**Fig. 9.** Fitted coefficients for spectral densities and coherence functions using data from anemometer A2–A7: (a) shape parameter for alongwind turbulence; (b) shape parameter for vertical wind turbulence; (c) coherence parameter for alongwind turbulence; (d) coherence parameter for vertical turbulence.

which is used to estimate the parameters $A_u$ and $A_w$ by fitting Eq. (43). These parameters are obtained by the least square fit $\text{argmin}_{A_u} \int_0^{1\,\text{Hz}} \left(\log_{10}(S_u(f, A_u)) - \log_{10}(S_u^{\text{Welch}}(f))\right)^2 \mathrm{d}f$, which is repeated similarly for $S_w(f, A_w)$. Fig. 8 shows the fit for a typical 10-min period, which indicates that a good model agreement is found. Fig. 9(a)–(b) shows the resulting coefficients for the whole

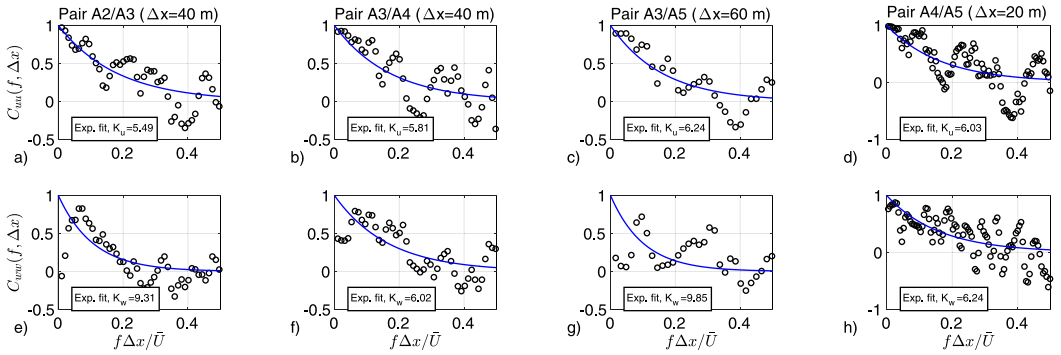


**Fig. 10.** Fit of exponential decay function for wind coherence for a typical 10-min period for anemometer pairs: (a–d): alongwind turbulence; (e–h): vertical turbulence.

time series. In general, a larger scatter is observed within one 10-min period for the vertical turbulence $w(t)$ than the horizontal turbulence $u(t)$, indicating weak inhomogeneity.

The coherence parameters $K_u$ and $K_w$ from Eq. (9) are also fitted using the cross-spectral density for each of the four anemometers pairs A2/A3, A3/A4, A3/A5, and A4/A5 with maximum interdistance $\Delta x \leq 60$ m. Also, these parameters are obtained by the least squares fit $\text{argmin}_{K_u} \int_0^{0.5} \left(C_{uu}(f, \Delta x, K_u) - C_{uu}^{\text{Welch}}(f, \Delta x)\right)^2 \mathrm{d}(f\Delta x/\bar{U})$ over the nondimensional frequency axis, and similarly for $C_{ww}(f, \Delta x, K_w)$. Fig. 10 shows a typical result. For most pairs, the curve fit is far from a perfect match. In fact, the estimation of coherence parameters is not a straightforward task since coherence models in wind engineering are known to be imperfect when compared to observations [49,50]. Fig. 9(c)–(d) show the resulting values for the whole time series. After discarding a few outlier values, $K_u$ and $K_w$ seem relatively consistent among the four cross-pairs. Although the obtained values for $K_u$ and $K_w$ agree well with a previous analysis of long-term data from this bridge [19], the coherence functions remain a significant source of uncertainty in the modelling of the wind field.

Finally, in the numerical modelling of the turbulent wind field for the whole bridge, the mean values for $\{\bar{U}, \sigma_u, \sigma_w, A_u, A_w, K_u, K_w\}$ as shown in Figs. 7 and 9 are for simplicity adopted for the whole span, thus assuming a homogeneous wind field. Note that, despite the introduced simplified assumptions such as stationary and homogeneity in the characterization of the wind field, the actual wind loads need not strongly conform to these assumptions. The inverse load estimation in the Kalman filter and RTS smoother is still strongly driven by the measured response data, which inevitably reflect the true and unidealized load conditions of the structure.

### 3.3. System submodels: finite element model and aeroelasticity model

As apparent from Eq. (2), the system model is separated into contributions from the structure and aeroelasticity. The structural part is generated from a FE model, where the still-air modes and corresponding natural frequencies are calculated. This is a FE model that was previously updated with respect to identified modal properties [51]. Proportional structural damping was adopted by using previously identified damping ratios, leading to the classic relations for the modal system matrices:

$$\tilde{\mathbf{M}}_0 = \mathbf{I}, \quad \tilde{\mathbf{C}}_0 = 2\boldsymbol{\Xi}_0\boldsymbol{\Omega}_0, \quad \tilde{\mathbf{K}}_0 = \boldsymbol{\Omega}_0^2 \tag{44}$$

where $\boldsymbol{\Omega}_0$ and $\boldsymbol{\Xi}_0$ are diagonal matrices assigned the (still-air) natural frequencies and damping ratios, respectively. A total of $n_m = 15$ vibrations modes are used, with natural frequencies from 0.05 Hz for the lowest and 0.41 Hz for the highest mode. The aeroelastic system contributions are found from modified quasi-steady theory [52], meaning that linearized distributed self-excited forces on the box girder in Fig. 1 can be expressed as:

$$\begin{bmatrix} q_{se,y}(x,t) \\ q_{se,z}(x,t) \\ q_{se,\theta}(x,t) \end{bmatrix} = \frac{1}{2}\rho\bar{U}(x,t)^2 \begin{bmatrix} p_4 & p_6 & p_3 B \\ h_6 & h_4 & h_3 B \\ a_6 B & a_4 B & a_3 B^2 \end{bmatrix} \begin{bmatrix} r_y(x,t) \\ r_z(x,t) \\ r_\theta(x,t) \end{bmatrix} + \frac{1}{2}\rho B\bar{U}(x,t) \begin{bmatrix} p_1 & p_5 & p_2 B \\ h_5 & h_1 & h_2 B \\ a_5 B & a_1 B & a_2 B^2 \end{bmatrix} \begin{bmatrix} \dot{r}_y(x,t) \\ \dot{r}_z(x,t) \\ \dot{r}_\theta(x,t) \end{bmatrix} \tag{45}$$

The 18 dimensionless coefficients $\{a_i, h_i, p_i\}$ $(i = 1 \ldots 6)$ are obtained from previous wind tunnel tests using a section model of the box girder [53] and are reported in Table 1. By integration along the span of the bridge, Eq. (45) leads to the following modal expressions for the aeroelastic stiffness and damping:

$$\tilde{\mathbf{K}}_{\text{ae}} = \int_0^L \frac{1}{2}\rho\bar{U}(x)^2\, \boldsymbol{\Phi}_{\text{ae}}(x)^{\text{T}} \begin{bmatrix} p_4 & p_6 & p_3 B \\ h_6 & h_4 & h_3 B \\ a_6 B & a_4 B & a_3 B^2 \end{bmatrix} \boldsymbol{\Phi}_{\text{ae}}(x)\, \mathrm{d}x \tag{46}$$

$$\tilde{\mathbf{C}}_{\text{ae}} = \int_0^L \frac{1}{2}\rho B\bar{U}(x)\boldsymbol{\Phi}_{\text{ae}}(x)^{\text{T}} \begin{bmatrix} p_1 & p_5 & p_2 B \\ h_5 & h_1 & h_2 B \\ a_5 B & a_1 B & a_2 B^2 \end{bmatrix} \boldsymbol{\Phi}_{\text{ae}}(x)\, \mathrm{d}x \tag{47}$$

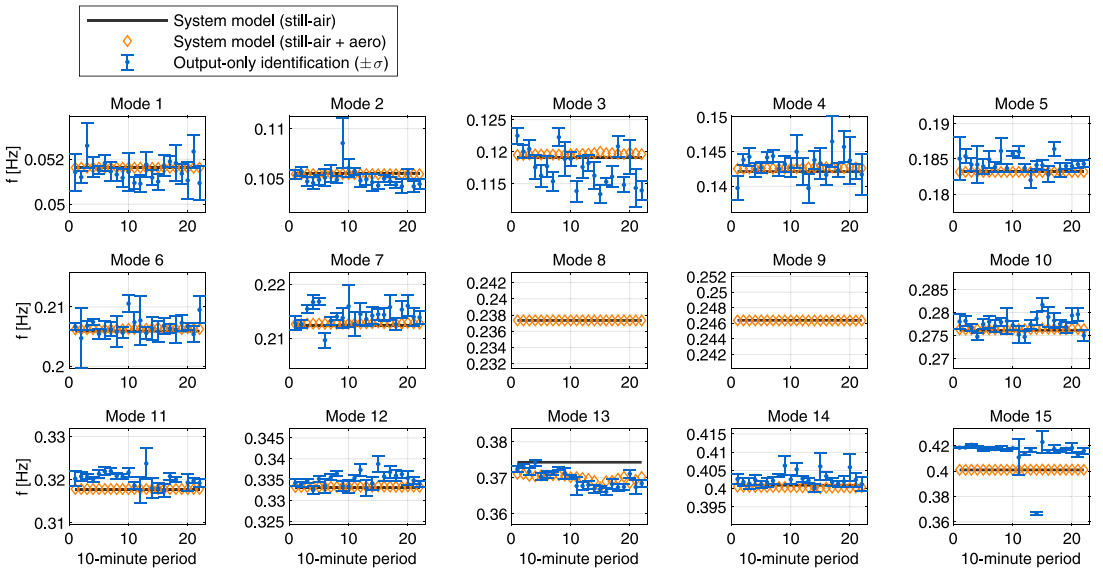


**Fig. 11.** Natural frequencies in the state space model compared to identified values. Two modes were not identified.

**Table 1**
Coefficients in modified quasi-steady theory for aeroelastic behaviour in bridges, wind tunnel tests of a section model of the Hardanger bridge.

| Variable | Value | Variable | Value | Variable | Value |
|---|---|---|---|---|---|
| $a_1$ | −0.853 | $h_1$ | −2.871 | $p_1$ | −0.313 |
| $a_2$ | −0.313 | $h_2$ | −0.081 | $p_2$ | −0.051 |
| $a_3$ | 0.907 | $h_3$ | 3.062 | $p_3$ | −0.030 |
| $a_4$ | −0.048 | $h_4$ | −0.379 | $p_4$ | 0.004 |
| $a_5$ | −0.015 | $h_5$ | 0.813 | $p_5$ | −0.247 |
| $a_6$ | 0.007 | $h_6$ | −0.055 | $p_6$ | −0.024 |

The effective modal properties obtained from the eigenvalues of $\mathbf{A}_c$ (see Eqs. (4) and (5)) are of particular interest to verify that is system model is adequate. Figs. 11 and 12 show the modelled natural frequencies and damping for the considered time series in 10-min discrete intervals, both the still-air values and the effective (in-wind) values that vary with $\bar{U}(t)$. It should be mentioned that the aeroelastic effects for the wind velocities under consideration mainly contribute to added damping; the change in natural frequencies is minor.

Since this is a study with operational (non-synthetic) data, some model imperfections are expected. Thus, for model verification purposes, an output-only system identification (covariance-based stochastic subspace identification [54]) is performed using the same time series. Note that this technique assumes a white noise excitation which strictly is violated in systems dominated by wind loads. This is overcome by overspecifying the model order in the modal identification, which separates the structural modes from spurious numerical modes arising from the coloured inputs (see e.g. [55]).

Figs. 11 and 12 also show identified damping ratios as estimated mean values and one standard deviation uncertainty bounds.

The shift in the natural frequencies due to aeroelastic stiffness is almost negligible but is still included here for completeness. As expected, the effective natural frequencies in the model mostly agree with the identified frequencies. On the other hand, (aeroelastic) damping is a far more complex (but vital) phenomenon that is more difficult both to model properly and identify from time series in operational modal analysis. Note that the uncertainty bounds in the identified damping values are quite wide compared to the frequencies. This can be expected in an operational case study where a number of uncertainties are present, such as measurement noise, limited length of data and slow variations in the mean wind velocity, which influences the aeroelastic damping. More detailed studies of environmental influences on damping for long-span bridges are worthy of further investigation but are not within the scope of this paper. The aerodynamic load coefficients used are reported in Table 2, which originate from state of the art wind tunnel tests of section models [53].

### *3.4. Latent force models*

As will be explained in the following, three different LFMs are tested as summarized in Table 3. LFM1 uses first-order Matérn kernels whose hyperparameters are obtained by a model fit to the predicted modal wind loads from the CWM (Appendix B). For the

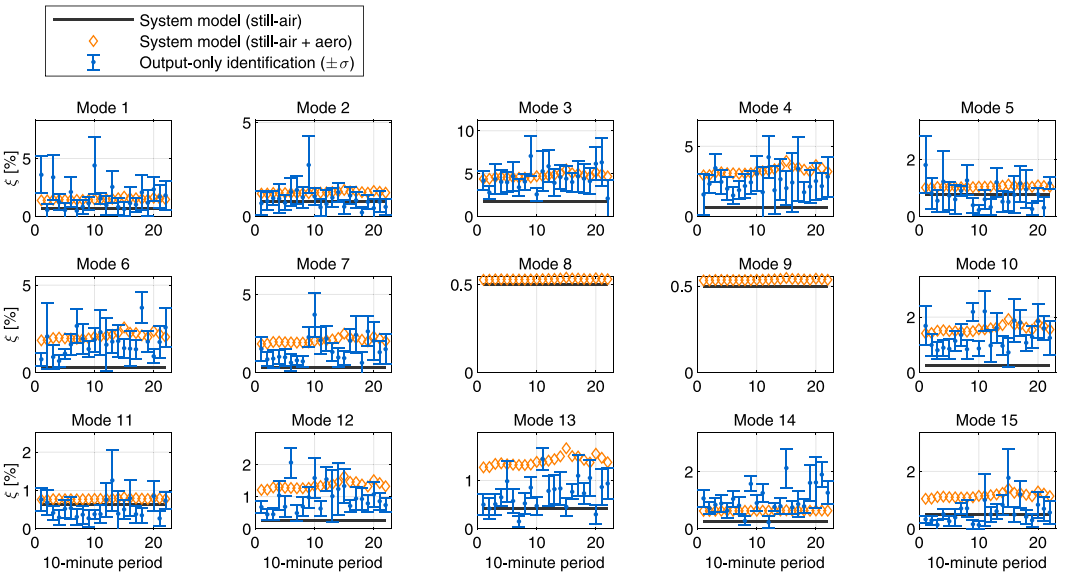


**Fig. 12.** Damping ratios in the state space model compared to identified values. Two modes were not identified.

**Table 2**
Values for bridge deck geometry in full scale, and linearized load coefficients for drag, lift, and pitching moment obtained from wind tunnel tests of a section model of the Hardanger bridge.

| Geometry | Value | Drag coeff. | Value | Lift coeff. | Value | Pitch coeff. | Value |
|---|---|---|---|---|---|---|---|
| $B$ | 18.3 m | $\bar{C}_D$ | 0.850 | $\bar{C}_L$ | −0.382 | $\bar{C}_M$ | 0 |
| $D$ | 3.25 m | $C'_D$ | 1.389 | $C'_L$ | 2.929 | $C'_M$ | 0.903 |

**Table 3**
The three different LFMs that are tested.

| Model no. | Tuning method | Kernel type | Tunable hyperparameters |
|---|---|---|---|
| LFM1 | Fit to predicted wind loads in CWM | 1st order Matérn | $\lambda_j \times 15$, $\sigma_{p,j} \times 15$ |
| LFM2 | Maximum likelihood of output data in Kalman filter | 1st order Matérn | $\sigma_p \times 1$, $\alpha_Q$, $\alpha_R$ |
| LFM3 | Maximum likelihood of output data in Kalman filter | 1st order Matérn | $\sigma_p \times 3$, $\alpha_Q$, $\alpha_R$ |

15 modes, this yields a total of 30 free hyperparameters. The corresponding fit of the covariance functions and spectral densities is shown for the 10-min period $t \in [6600, 7200]$ in Figs. 13 and 14, and a similar goodness of fit is obtained for the other time periods.

Whereas LFM1 is directly specified based on prior engineering assumptions (i.e. physical models), LFM2 and LFM3 are tuned by maximum likelihood methods as explained in the following. Neglecting constants, the log marginal likelihood of the output data given the hyperparameter set, commonly written in the notation $p(\mathbf{y}_{[1:N]}|\boldsymbol{\theta})$, is given as follows [56]:

$$\log(L) = -\frac{1}{2}\sum_{k=1}^{N}\left(\log(|\mathbf{S}_k|) + \mathbf{e}_k^T\mathbf{S}_k^{-1}\mathbf{e}_k\right) \tag{48}$$

Here, $\mathbf{S}_k$ is the covariance matrix of the innovation vector $\mathbf{e}_k$ in the Kalman filter; see Eqs. (A.1) and (A.2) in Appendix A. The objective function in Eq. (48) intrinsically balances the trade-off between the penalties related to the complexity and the fit to the observed data. This approach does require the number of hyperparameters to be limited in order to reduce computational time. The choice of parameterization is not trivial, however.

As an initial example, consider for simplicity the case where the same value of $\lambda$ and $\sigma_p$ is used for all modal loads. Using data from a typical 10-min period, Fig. 15 shows a plot of the negative log-likelihood function for a naive grid search where $\lambda$ and $\sigma_p$ are varied with fixed logarithmic spacing. In Fig. 15(a), a diagonal ridge is observed where the log-likelihood function is equally optimal, so no distinct hyperparameter solution can be preferred. Along this ridge, the value of $\lambda\sigma_p^2$ is constant. In fact, in GP regression, it is known that neither $\lambda$ or $\sigma_p$ for the Matérn covariance function (in Eq. (26)) can be consistently estimated, only the product $\lambda\sigma_p^2$ [57,58] (for data in a bounded region, aka. fixed-domain asymptotics). Furthermore, for a chosen fixed value $\lambda^*$, the estimate of $\lambda^*\hat{\sigma}_p^2$ will converge towards the true value of $\lambda\sigma_p^2$. The state and load estimates are not necessarily equal for all pairs $\{\lambda, \sigma_p\}$ on this ridge, however. For instance, if one chooses a small $\lambda$ (and correspondingly large $\sigma_p$), spurious low-frequent fluctuation is introduced in the state and load estimates, as $\lambda$ dictates the tail behaviour of the spectral density in Eq. (25) when $\omega$ is close to zero.

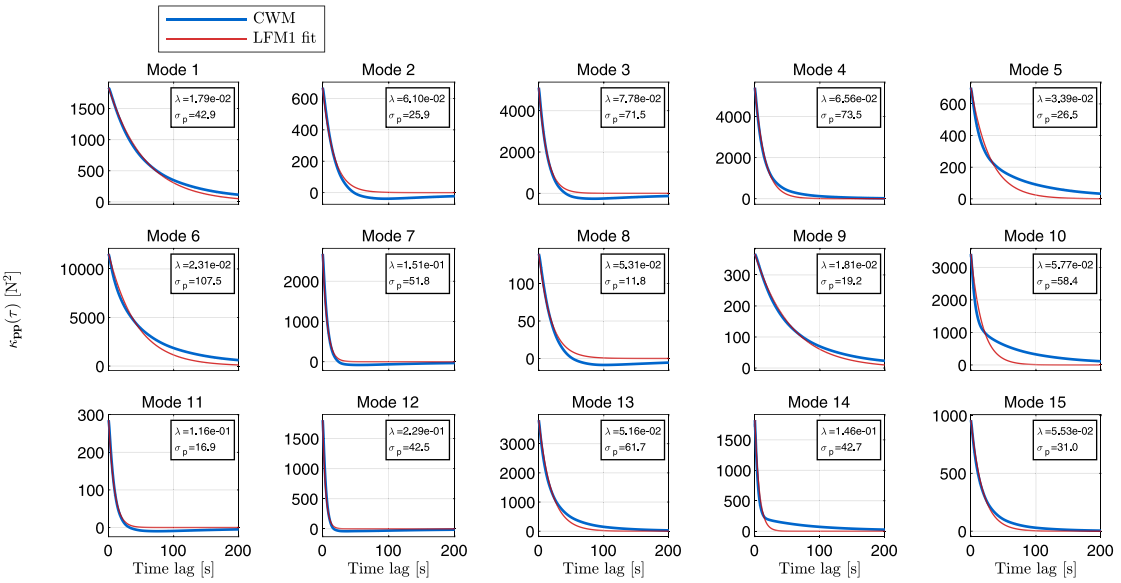


**Fig. 13.** Covariance functions of the modal loads from the CWM compared to the fitted LFM1 with a Matérn kernel. Results are taken from a typical 10-min period.

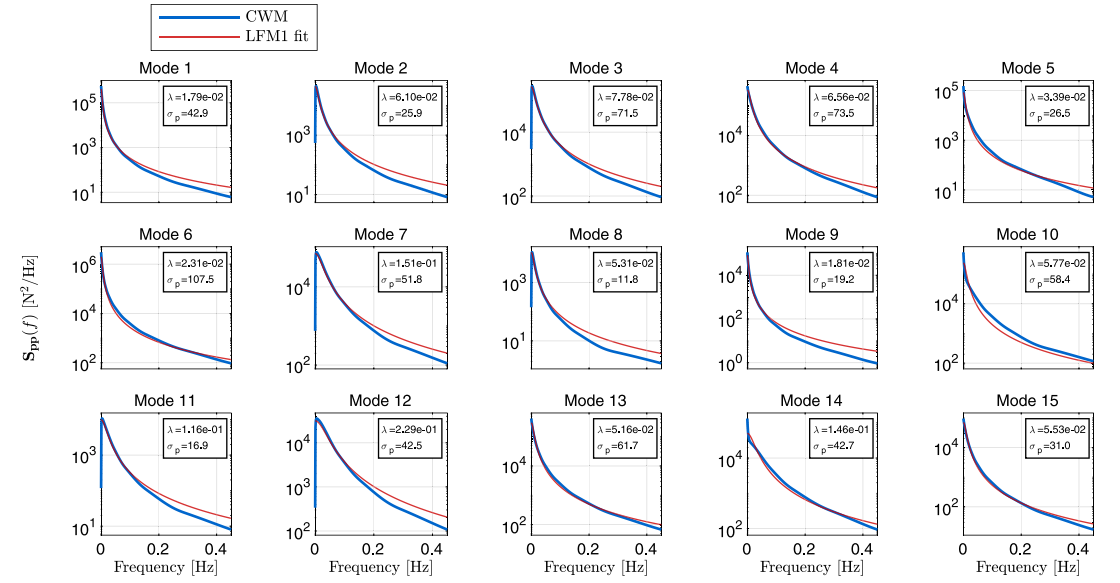


**Fig. 14.** One-sided spectral density of the modal loads from the CWM compared to the fitted LFM1 with a Matérn kernel. Results are taken from a typical 10-min period.

One option is to consider a fixed value $\lambda^*$ and then find the optimal estimate for $\hat{\sigma}_p$ only. This approach also leads to fewer optimization variables, which reduces the computational burden. At the same time, this also means that some physical significance of the covariance function is lost since the estimate $\hat{\sigma}_p$ then depends on the guessed value $\lambda^*$. This is not necessarily a limitation, as in applications of GP regression, the hyperparameters are not always rooted in a direct physical meaning but merely used as optimal values that best fit the underlying structure of the given data set. For this reason, LFM2 and LFM3 utilize the fixed values for $\lambda$ from LFM1. The magnitude factor $\sigma_p$ is kept as a free hyperparameter; in LFM2, the same value is used for all modal loads. In LFM3, $\sigma_p$ is shared within the following three groups: (i) lateral and torsional modes, (*ii*) vertical modes, and (*iii*) other modes. This choice is made because the modal loads within these groups roughly tend to have the same magnitude.

In addition, the values of $\mathbf{R}$ and $\mathbf{Q}_{\mathrm{xd}}$ are included as tunable parameters by the scale factors $\alpha_Q$ and $\alpha_R$, as the magnitudes of these covariance matrices are also found to influence the likelihood function. This yields a total of three and five tunable hyperparameters in LFM2 and LFM3, respectively, which is summarized in Table 3. The likelihood function can also suffer from solutions that are

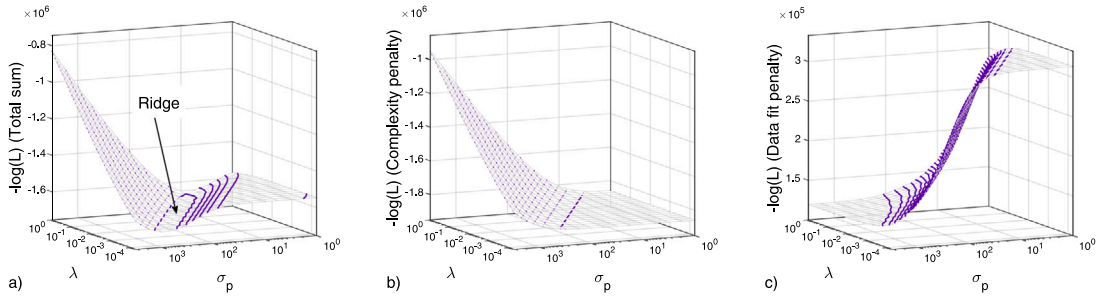


**Fig. 15.** Grid search of $-\log(L)$ by varying $\lambda$ and $\sigma_p$. The values of the covariance matrices $\mathbf{Q}_{\text{xd}}$ and $\mathbf{R}$ are fixed. The purple lines are isolines. (a) the negative likelihood function $-\log(L)$; (b) contribution from the model complexity penalty term ($\log(|\mathbf{S}_k|)$ in Eq. (48)); (c) contribution from the data fit penalty term ($\mathbf{e}_k^T\mathbf{S}_k^{-1}\mathbf{e}_k$ in Eq. (48)).

only locally optimal, so a broad search considering multiple initial points was employed to locate the global optimum with a high degree of confidence. To this end, the *GlobalSearch* function in Matlab was used, which was configured to run the gradient-based minimization routine *fmincon* for 100 random initial points. In order to ease the optimization and prevent unreasonable initial points, parameter bounds were enforced. These were selected as $[10^{-3}, 10]$ for $\lambda$ and $[10^{-1}, 10^{3}]$ for $\sigma_p$, which corresponds approximately lower and upper limits respectively $1/100$ and 100 times the parameter values that were predicted by the CWM. Similarly, $\alpha_Q$ and $\alpha_R$ were bounded between $1/100$ and 100.

### 3.5. Identification of wind loads and global responses for initial and optimized latent force models

When the augmented state-space models are established, the state estimation is performed with a classic Kalman filter (KF) [45] and subsequently a backward Rauch–Tung–Striebel (RTS) smoother [46]. Only acceleration data is used in the output vector ($\mathbf{S}_{\text{disp}} = \mathbf{0}$). The data from two sensors in the mid span (H5E and H5W, see Fig. 4) are not included in the output but left as reference data for virtual sensing comparisons. The state $\mathbf{x}_0^{\text{a}}$ is set to zero initially, and the steady-state solutions in the KF and RTS algorithms are used to process each 10-min interval of data sequentially.

The tuning of the covariance matrices is known to be important, as they must account for additional (white noise) excitation, model errors, and sensor noise. For LFM1, the covariance matrices are initially tuned manually; $\mathbf{R} = 10^{-6} \cdot \mathbf{I}$ is assigned to the measurement errors and $\mathbf{Q}_{\text{xd}}$ is set to $10 \cdot \mathbf{I}$. LFM2 and LFM3 use the same covariance matrices but are scaled by tunable hyperparameters, i.e. $\alpha_R\mathbf{R}$ and $\alpha_Q\mathbf{Q}_{\text{xd}}$. A diagonal structure is used for these covariance matrices due to lack of knowledge to the nature and form of the unmodelled dynamics and noises that may be present in the data. Prospects for better suited and robust alternatives are, in our opinion, a point of possible improvement in the application of stochastic state-space models to complex cases where the residual dynamics are not fully understood.

The estimated modal forces are shown in Fig. 16. Although a direct verification of these estimates is nearly impossible, it is possible to distinguish the load effect of strong wind gusts; in swift comparison with Fig. 6, it can be seen that the largest loads appear approximately concurrently with strong wind gusts, which is expected. A zoom of the load estimates is shown in Fig. 17, where one standard deviation of uncertainty is also superimposed, which is obtained from the covariance of the smoothing estimate (see Eq. (A.10)). This type of uncertainty quantification is a strength of the identification methods based on Kalman filters. The uncertainty seems to greatly vary between the estimated from different LFMs, mostly since these uncertainties depend on the variation in the tuned noise statistics $\mathbf{R}$ and $\mathbf{Q}_{\text{ad}}$ (see Section 3.6), which are not always easy to define for structures where model errors, additional excitation, and sensor noise all simultaneously play a role. Similarly, Fig. 18 shows the state estimate for the lowermost six modes with standard deviation uncertainty bounds. Also here uncertainty variation between the LFMs are observed. Nevertheless, the uncertainty appears to be rather small for some components, such as mode 1, and relatively large for others, such as modes 5 and 6.

Unfortunately, displacement measurements are not incorporated in this monitoring system. The validity of the state estimates can, to some extent, still be probed via an estimation of displacements in the bridge deck, denoted as $\hat{\mathbf{r}}(t)$. This quantity is obtained directly from the state estimate as follows by selecting the desired DOFs with the matrix $\mathbf{S}'$:

$$\hat{\mathbf{r}}(t) = \begin{bmatrix}\mathbf{S}'\boldsymbol{\Phi} & \mathbf{0}\end{bmatrix}\hat{\mathbf{x}}(t) \tag{49}$$

The displacements in the mid span are examined in Fig. 19. This figure also shows the pseudo displacements obtained from the direct numerical integration of the acceleration data from sensors at this position (H5E and H5 W, see Fig. 4). This exercise requires a carefully designed high-pass filter (Chebyshev Type II, 0.025 Hz stopband frequency) that eliminates the accumulated integration errors but does not disturb the dynamic content from the lowest vibration mode at 0.05 Hz. In bridge aerodynamics, it is common to evaluate bridge deck responses in terms of lateral, vertical, and torsion motion. For a clearer illustration of these degrees of freedom, the signals from the sensors pair in the mid span are transformed into a lateral, vertical and torsional component for the reference point in the centre of the bridge deck (see Fig. 1).

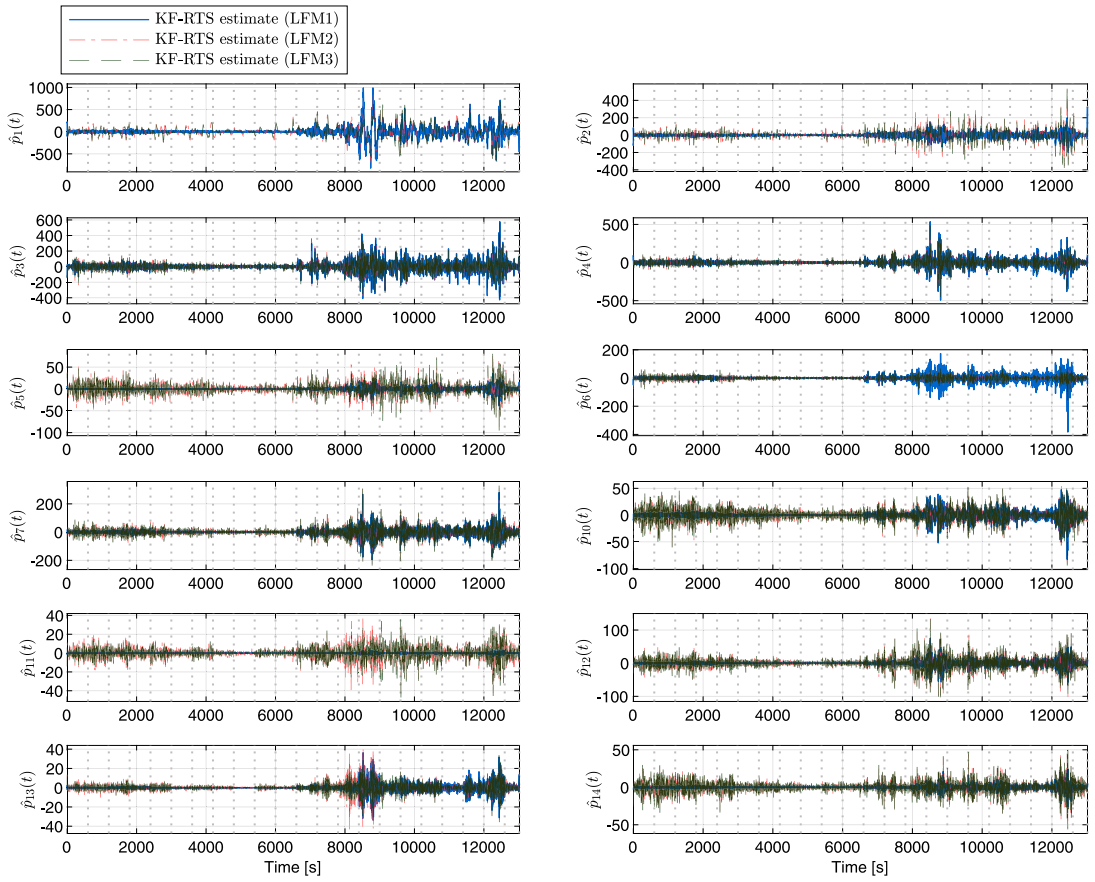


**Fig. 16.** Time history of estimated modal forces.

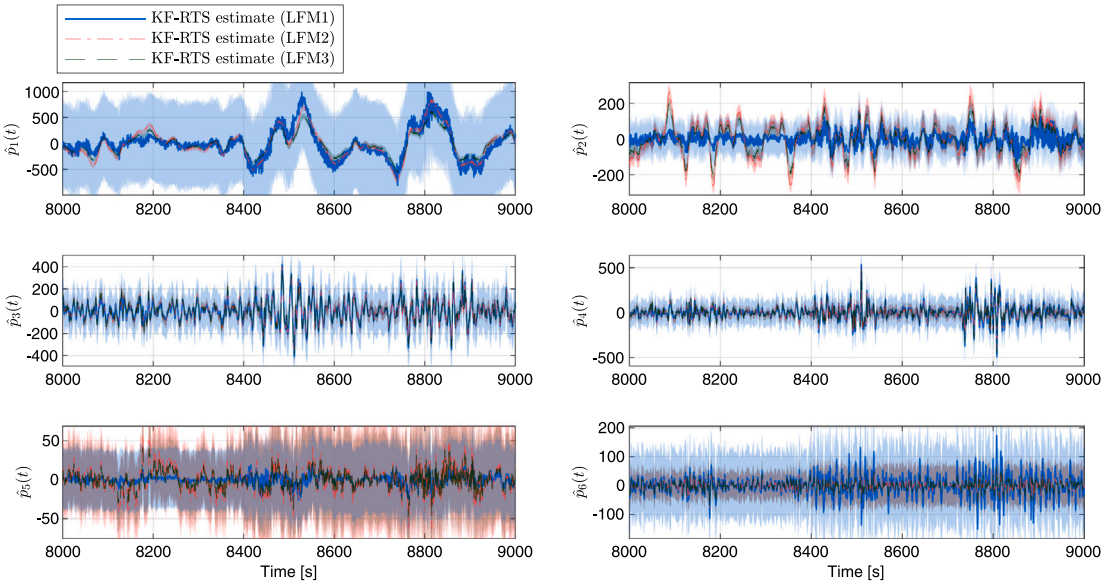


**Fig. 17.** Modal load estimates for mode 1–6 (zoomed time axis) with one standard deviation of uncertainty.

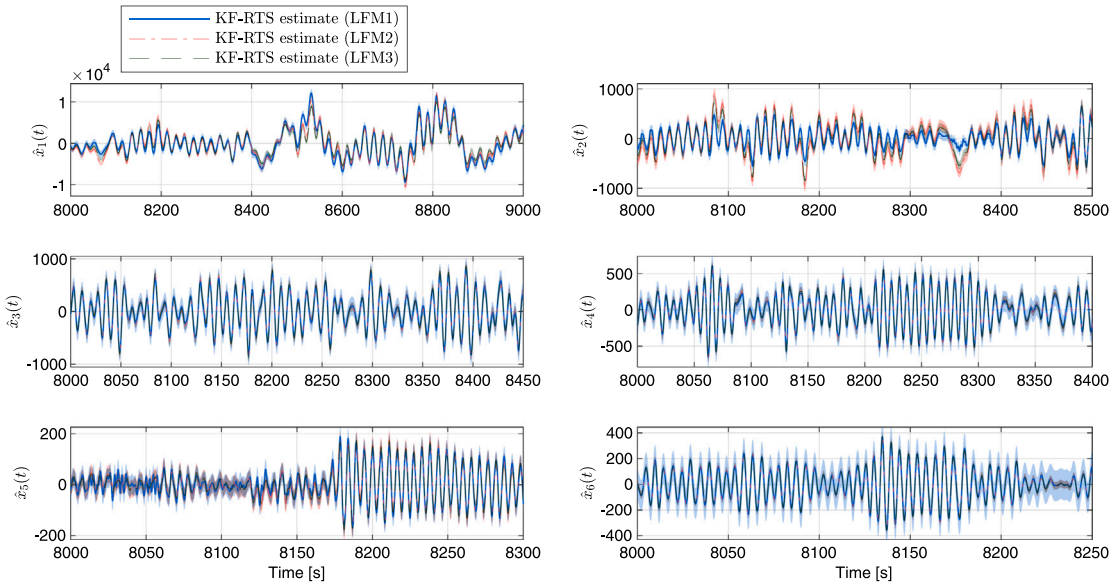


**Fig. 18.** State estimates for mode 1–6 (zoomed time axis) with one standard deviation of uncertainty.

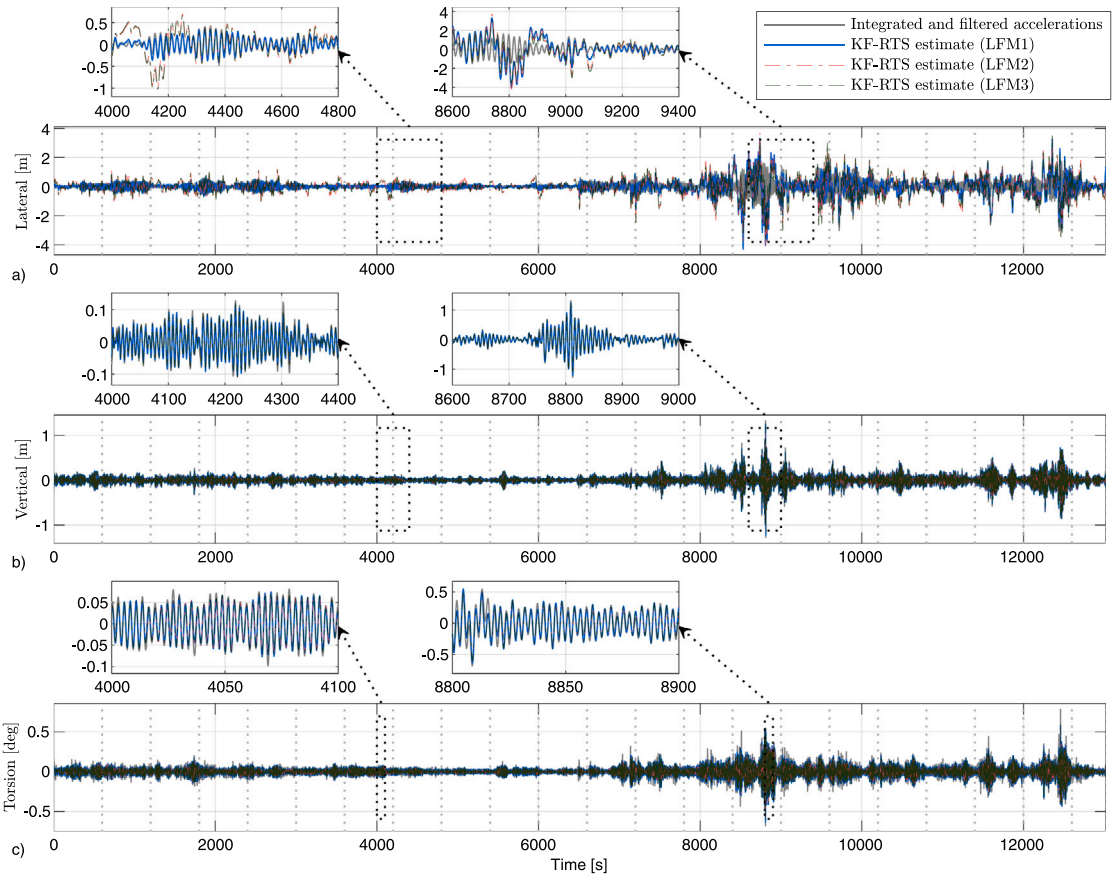


**Fig. 19.** Time history of estimated response in the mid span of the bridge: (a) lateral displacement; (b) vertical displacement; (c) torsional rotation.

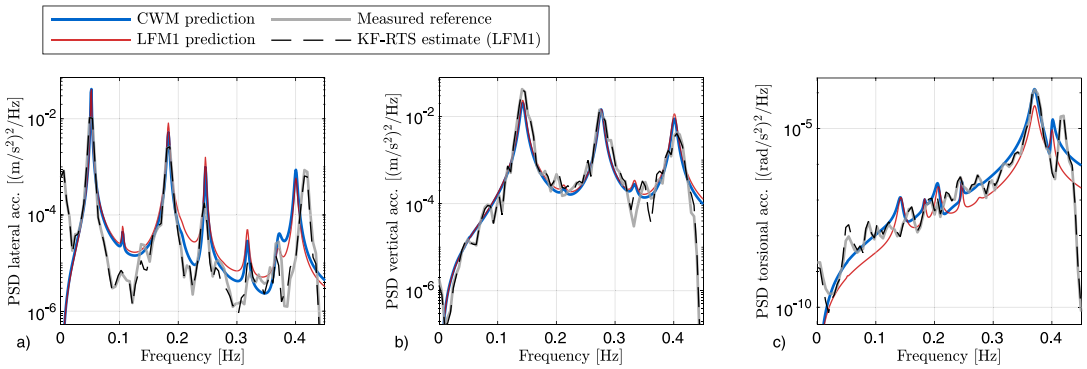


**Fig. 20.** Spectral density of the bridge deck at mid-span for the 10-min period $t \in [4800, 5400]$ s: (a) lateral acceleration; (b) vertical acceleration; (c) torsional acceleration.

As expected, state estimates and the direct integration lead to similar time histories, except for the lateral displacements in Fig. 19(a). In [8] it was shown that fusion of the LFMs into Kalman filters eliminates the instabilities that would otherwise occur in the case of acceleration output only, which is also confirmed here. This theoretical result does not exclude the possibility that in reality some low-frequency fluctuations in the estimates can still occur due to insensitivity in the accelerometers to quasi-static behaviour, which can be caused by slow-varying changes in the wind velocity. For this bridge, this mainly influences the lateral motion and not the vertical or torsional motion of the bridge deck shown in Fig. 19(b)–(c). The resonance component in Fig. 19(a), which is dominated by the lowest natural frequency with a period 20 s, still seems well represented. To obtain a complete response reconstruction of the wind loads, some static reference measurements (such as strains, inclinations, or GPS data) could still be preferred.

A further validation of the obtained displacement results is highly desirable but currently not feasible due to the lack of data from this bridge. The authors have also recently instrumented another suspension bridge of similar scale where also strain gauges have been included in the sensor network [59], which may give further insight into the low-frequent wind-induced response behaviour.

Next, the difference between the predicted response and the actual response of the bridge is highlighted. Since the CWM and LFM treat the loads and responses as stochastic and stationary, comparisons with the actual bridge response are performed in the frequency domain using spectral densities. As discussed in Section 2.2, the introduction of LFMs into the KF-RTS load estimation implies that an assumed spectral density for the loads (Eq. (29)) is adopted, hence it is also implicitly assumed a prior form of spectral density for the bridge response.

Figs. 20 and 21 compare the acceleration spectral density in the mid-span for two different 10-min periods. These figures also show the spectral density of the measured accelerations and the extrapolated accelerations from the KF-RTS in the same degrees of freedom, where Welch's method has been applied to the time-domain signals to produce the spectra. In Fig. 20, the prediction from the CWM matches the measured accelerations quite well. Thus the environmental load model is a decent predictor for the actual bridge response for this 10-min period. A different situation is observed in Fig. 21, where the measured accelerations are generally much greater than the spectral density from the predictions that rely on environmental and aerodynamic data. This is true in particular for the vertical (Fig. 21b) and torsional (Fig. 21c) motion, but also to some extent for the lateral motion (Fig. 21a). This result reflects the level of uncertainty in the current load models wind engineering, and their propagation to bridge response predictions. It is noted that the accelerations that are extrapolated from the KF-RTS unsurprisingly match well with the measured reference accelerations. Thus, the nominal response prediction from the LFM serves as a prior which can effectively be updated in the KF-RTS routine with the information provided by the measured acceleration.

Note that there are also small but notable disparities between the LFM1 and CWM predictions in Figs. 20 and 21; the peak values at the natural frequencies have slight differences in their magnitudes. This again comes down to the fitting of covariance functions in LFM1, and as shown in Fig. 14 small differences in the two models are present. As an alternative to the proposed LFM fitting that is applied here (Appendix B), one could also choose to emphasize the LFM frequency content for each modal load around its natural frequency, as this band accounts for most of the contribution to the modal response.

### 3.6. Optimized hyperparameters

It is also interesting to compare the obtained values for the hyperparameters. Fig. 22(a)–(c) shows the hyperparameter $\sigma_p$ for all LFMs. Interestingly, for the lateral modes (Fig. 22(a)), the optimal values in LFM2 and LFM3 are very close to the mean value for all modes from LFM1. For the vertical modes in Fig. 22(b), a larger discrepancy is seen; LFM2 and LFM3 both consistently yield lower values than predictions from the CWM in LFM1. The scale factors for the covariance matrices in Fig. 22(d)–(e) also change a fairly large amount, which could be expected since the initial covariance values were crudely and manually tuned initially. As noted by other researchers [11], the spectral density of the LFM (and thus indirectly the hyperparameters) does not necessarily match the spectral density of the actual forces since the model can prefer that the excitation is partly modelled by the added white noise terms

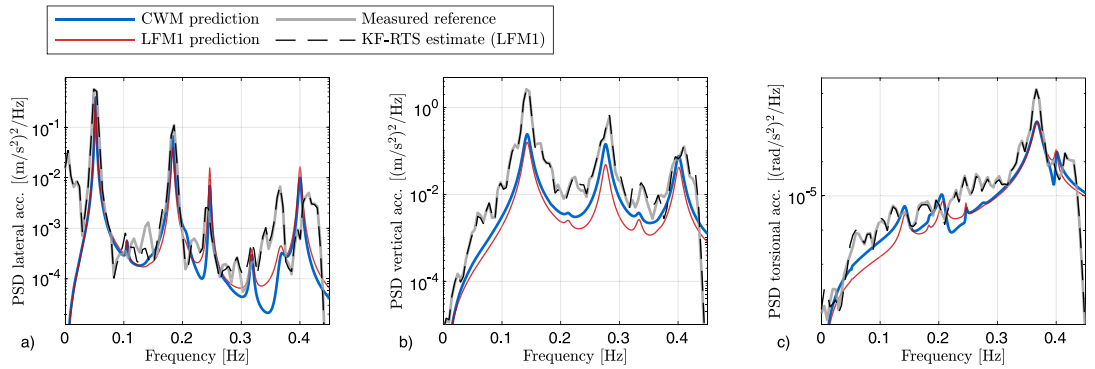


**Fig. 21.** Spectral density of the bridge deck at mid-span for the 10-min period $t \in [8400, 9000]$ s: (a) lateral acceleration; (b) vertical acceleration; (c) torsional acceleration.

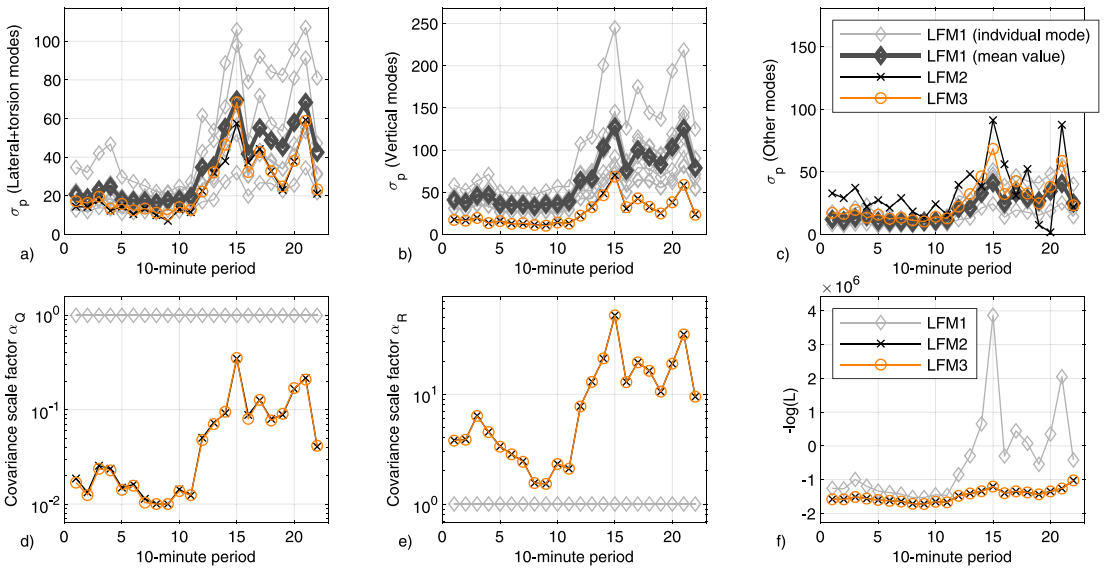


**Fig. 22.** (a)–(e): Hyperparameters; (f): negative likelihood objective function Eq. (48).

in Eq. (37). It should be mentioned that recently proposed methods also attempt an updating of the covariance matrices within the Kalman filter [6]. However, this was not attempted here.

Fig. 22(f) shows the negative log-likelihood function (Eq. (48)) for all three LFMs. Note that LFM1 is not optimized with respect to this objective function but is still included here for comparison. LFM2 and LFM3 generally perform equally well, even though the number of hyperparameters is different, which illustrates that a compressed set of hyperparameters may yield satisfactory results compared to a more complicated model. Furthermore, whereas LFM2 and LFM3 are comparably equal to LFM1 in the first half of the time series (period 1–11 and onwards), the greatest change in the objective function occurs in the last half (period 12 and onwards). This trend also coincides with the periods with the most violent gusts in Fig. 6, which may indicate that these periods have the largest discrepancies between the real data and the underlying predictions from the CWM, which was used in LFM1. The CWM is a prediction based on idealized linear theory, and Eq. (6) neglects, for instance, higher-order effects of the wind loading such as terms proportional to the turbulence squared ($u(x,t)^2$ and $w(x,t)^2$). This is an appealing argument as to why the identification of wind loads could bring further refinement in the characterization of wind loads and wind-induced responses.

## 4. Conclusions

In this paper, an application of inverse estimation for wind loads on bridges was presented. The use of GP-LFMs in Kalman filter-based force identification was explored. Specifically, it was proposed to design the LFMs using information from existing wind loads models based on aerodynamic coefficients from wind tunnel tests and wind parameters from the structural monitoring system of the bridge.

In a case study, using data from the Hardanger Bridge, the modal responses and modal wind loads were estimated from measured accelerations. The use of physics-informed GP-LFMs in force identification gives the possibility to include prior knowledge about the unknown forces while still actively depending on the measured responses for the reconstruction of the actual dynamic behaviour. Several LFMs with first-order Matérn kernels were tested, which were tuned by standard evidence methods of log-likelihood maximization. The results showed that the complexity of the LFMs can be kept low; simple models with relatively few free hyperparameters yields satisfactory estimates. It was found that the estimation is stable for acceleration output only, although static measurements could still be preferred to accurately capture the effects of quasi-static wind loads.

## CRediT authorship contribution statement

**Ø.W. Petersen:** Methodology, Software, Data curation, Formal analysis, Writing – original draft. **O. Øiseth:** Funding acquisition, Data curation, Writing – review & editing. **E. Lourens:** Writing – review & editing.

## Declaration of competing interest

The authors declare that they have no known competing financial interests or personal relationships that could have appeared to influence the work reported in this paper.

## Acknowledgement

This research was financially supported by the Norwegian Public Roads Administration. The authors appreciate this support.

## Appendix A. Equations for Kalman filter and RTS smoother

The following summarizes the equations for filtering and smoothing for the system model in Eqs. (37) and (38) with the notation used in this paper. The notation $\hat{\mathbf{x}}^{\mathrm{a}}_{k|l}$ for the augmented state denotes the estimate at time step $k$ using observation data up to time step $l$; the associated covariance matrix is denoted as $\hat{\mathbf{P}}^{\mathrm{a}}_{k|l}$. The filter is initiated by the prior estimate $\hat{\mathbf{x}}^{\mathrm{a}}_{1|0}$ for the augmented state and covariance matrix $\mathbf{P}^{\mathrm{a}}_{1|0}$. Note that the Kalman filter has a steady-state solution that can be found by the discrete algebraic Ricatti equation (see, for instance, [60,61]) so that the matrices $\mathbf{S}_k$, $\mathbf{K}_k$, $\mathbf{P}^{\mathrm{a}}_{k|k}$, and $\mathbf{P}^{\mathrm{a}}_{k+1|k}$ need only be calculated once. Likewise, Lyaponov equations for the RTS smoother yields the steady-state solution for the matrices $\mathbf{N}_k$ and $\mathbf{P}^{\mathrm{a}}_{k|N}$.

Kalman filter, measurement update ($k = 1, 2, \dots, N$):

$$\mathbf{e}_k = \mathbf{y}_k - \mathbf{H}_{\mathrm{ad}}\hat{\mathbf{x}}^{\mathrm{a}}_{k|k-1} \tag{A.1}$$

$$\mathbf{S}_k = \mathbf{H}_{\mathrm{ad}}\mathbf{P}^{\mathrm{a}}_{k|k-1}\mathbf{H}^{\mathrm{T}}_{\mathrm{ad}} + \mathbf{R} \tag{A.2}$$

$$\mathbf{K}_k = \mathbf{P}_{k|k-1}\mathbf{H}^{\mathrm{T}}_{\mathrm{ad}}\mathbf{S}^{-1}_k \tag{A.3}$$

$$\hat{\mathbf{x}}^{\mathrm{a}}_{k|k} = \hat{\mathbf{x}}^{\mathrm{a}}_{k|k-1} + \mathbf{K}_k\mathbf{e}_k \tag{A.4}$$

$$\mathbf{P}^{\mathrm{a}}_{k|k} = \mathbf{P}^{\mathrm{a}}_{k|k-1} - \mathbf{K}_k\mathbf{S}_k\mathbf{K}^{\mathrm{T}}_k \tag{A.5}$$

Kalman filter, time update:

$$\hat{\mathbf{x}}^{\mathrm{a}}_{k+1|k} = \mathbf{F}_{\mathrm{ad}}\hat{\mathbf{x}}^{\mathrm{a}}_{k|k} \tag{A.6}$$

$$\mathbf{P}^{\mathrm{a}}_{k+1|k} = \mathbf{F}_{\mathrm{ad}}\mathbf{P}^{\mathrm{a}}_{k|k}\mathbf{F}^{\mathrm{T}}_{\mathrm{ad}} + \mathbf{Q}_{\mathrm{ad}} \tag{A.7}$$

Rauch–Tung–Striebel smoother, backward pass ($k = N, N-1, \dots, 1$):

$$\mathbf{N}_k = \mathbf{P}^{\mathrm{a}}_{k|k}\mathbf{F}^{\mathrm{T}}_{\mathrm{ad}}(\mathbf{P}^{\mathrm{a}}_{k+1|k})^{-1} \tag{A.8}$$

$$\hat{\mathbf{x}}^{\mathrm{a}}_{k|N} = \hat{\mathbf{x}}^{\mathrm{a}}_{k|k} + \mathbf{N}_k(\hat{\mathbf{x}}^{\mathrm{a}}_{k+1|N} - \hat{\mathbf{x}}^{\mathrm{a}}_{k+1|k}) \tag{A.9}$$

$$\mathbf{P}^{\mathrm{a}}_{k|N} = \mathbf{P}^{\mathrm{a}}_{k|k} + \mathbf{N}_k(\mathbf{P}^{\mathrm{a}}_{k+1|N} - \mathbf{P}^{\mathrm{a}}_{k+1|k})\mathbf{N}^{\mathrm{T}}_k \tag{A.10}$$

## Appendix B. Equations for fit of first-order LFMs

Consider a stationary process $f(t)$, which is modelled by the first-order stochastic differential equation:

$$\dot{f}(t) = -\lambda f(t) + \tilde{w}(t) \tag{B.1}$$

where $\sigma^2_{\tilde{w}}$ is the variance of the stochastic Gaussian noise $\tilde{w}(t)$. Eq. (B.1) can be converted to discrete time with intersample time $h$, which forms an autoregressive (AR) model of order 1:

$$f_{k+1} = \phi_1 f_k + \tilde{w}_k \tag{B.2}$$

where the AR(1) coefficient is $\phi_1 = \exp(-\lambda h)$. The variance of $\tilde{w}_k$ is given by [62]:

$$\mathbb{E}[\tilde{w}_k^2] = \frac{\sigma^2_{\tilde{w}}}{2\lambda}(1 - \exp(-2\lambda h)) = \frac{\sigma^2_{\tilde{w}}}{2\lambda}(1 - \phi_1^2) \tag{B.3}$$

Next, we wish to fit the parameters of the AR model, assuming that an autocovariance function $\kappa_f(\tau)$ for $f(t)$ is available, which can be estimated from observed data or obtained from physical models. The parameter estimation is performed by the method of moments. When Eq. (B.2) is multiplied by $f_k$, the following is obtained:

$$\mathbb{E}[f_k f_{k+1}] = \phi_1 \mathbb{E}[f_k^2] + \mathbb{E}[\tilde{w}_k f_k] \tag{B.4}$$

Since $\tilde{w}_k$ and $f_k$ are uncorrelated, the AR(1) coefficient estimate can simply be expressed as:

$$\hat{\phi}_1 = \frac{\mathbb{E}[f_k f_{k+1}]}{\mathbb{E}[f_k^2]} = \frac{\kappa_f(h)}{\kappa_f(0)} \tag{B.5}$$

The same result is obtained by the well-known Yule–Walker equations for AR models [63]. The corresponding estimate for $\lambda$ thus becomes:

$$\hat{\lambda} = -\frac{1}{h}\log(\hat{\phi}_1) = -\frac{1}{h}\log(\frac{\kappa_f(h)}{\kappa_f(0)}) \tag{B.6}$$

The noise parameter variance can be found from Eq. (B.2) by squaring this equation:

$$\mathbb{E}[(f_{k+1} - \phi_1 f_k)^2] = \mathbb{E}[f_{k+1}^2] + \phi_1^2 \mathbb{E}[f_k^2] - 2\phi_1 \mathbb{E}[f_k f_{k+1}] = \mathbb{E}[\tilde{w}_k^2] \tag{B.7}$$

Because of stationarity, $\mathbb{E}[f_{k+1}^2] = \mathbb{E}[f_k^2] = \kappa_f(0)$. From Eq. (B.4) it is seen that $\mathbb{E}[f_k f_{k+1}] = \phi_1 \mathbb{E}[f_k^2]$. Combined with Eq. (B.3) and (B.7) this lead to leads to:

$$\kappa_f(0)(1 - \phi_1^2) = \frac{\sigma^2_{\tilde{w}}}{2\lambda}(1 - \phi_1^2) \tag{B.8}$$

so that the estimate of the new parameter $\sigma_p^2 = \sigma^2_{\tilde{w}}/(2\lambda)$ simply becomes:

$$\hat{\sigma}_p^2 = \kappa_f(0) \tag{B.9}$$

Eq. (B.5) has the drawback that it only considers one time lag ($\tau = h$), which can give a poor fit for long memories. To obtain a better fit, a broader estimation can be performed by considering a time lag up to $\tau = mh$, where the integer $m \geq 1$ must be chosen. The expression for the covariance function of the AR(1) model is $R_f(kh) = \phi_1^k R_f(0)$, where the integer $k \geq 1$. It is possible to consider a system of $m$ time lags as follows:

$$\begin{bmatrix} R_f(0) \\ R_f(h) \\ \vdots \\ R_f((m-1)h) \end{bmatrix} \phi_1 = \begin{bmatrix} R_f(h) \\ R_f(2h) \\ \vdots \\ R_f(mh) \end{bmatrix} \tag{B.10}$$

or compactly

$$\mathbf{\Gamma_m}\phi_1 = \boldsymbol{\gamma_m} \tag{B.11}$$

When $\mathbf{\Gamma_m}$ and $\boldsymbol{\gamma_m}$ are populated with the autocovariance function $\kappa_f(\tau)$, Eq. (B.10) represents an overdetermined system, which can be solved in the least square sense for $\phi_1$ by the pseudo-inverse operation:

$$\hat{\phi}_1 = (\mathbf{\Gamma_m}^{\mathrm{T}}\mathbf{\Gamma_m})^{-1}\mathbf{\Gamma_m}^{\mathrm{T}}\boldsymbol{\gamma_m} \tag{B.12}$$

The above equations can also be extended to fitting of AR models of higher orders [64], although only the first-order AR model is used in this paper.

## References


[1] N.M. Okasha, D.M. Frangopol, Integration of structural health monitoring in a system performance based life-cycle bridge management framework, Struct. Infrastruct. Eng. 8 (11) (2012) 999–1016.
[2] S.E. Azam, E. Chatzi, C. Papadimitriou, A dual Kalman filter approach for state estimation via output-only acceleration measurements, Mech. Syst. Signal Process. 60 (2015) 866–886.
[3] E.-M. Lourens, C. Papadimitriou, S. Gillijns, E. Reynders, G. De Roeck, G. Lombaert, Joint input-response estimation for structural systems based on reduced-order models and vibration data from a limited number of sensors, Mech. Syst. Signal Process. 29 (2012) 310–327.
[4] E.-M. Lourens, E. Reynders, G. De Roeck, G. Degrande, G. Lombaert, An augmented Kalman filter for force identification in structural dynamics, Mech. Syst. Signal Process. 27 (2012) 446–460.
[5] K. Maes, S. Gillijns, G. Lombaert, A smoothing algorithm for joint input-state estimation in structural dynamics, Mech. Syst. Signal Process. 98 (2018) 292–309.
[6] O. Sedehi, C. Papadimitriou, D. Teymouri, L.S. Katafygiotis, Sequential Bayesian estimation of state and input in dynamical systems using output-only measurements, Mech. Syst. Signal Process. 131 (2019) 659–688.
[7] W. Song, Generalized minimum variance unbiased joint input-state estimation and its unscented scheme for dynamic systems with direct feedthrough, Mech. Syst. Signal Process. 99 (2018) 886–920.
[8] R. Nayek, S. Chakraborty, S. Narasimhan, A Gaussian process latent force model for joint input-state estimation in linear structural systems, Mech. Syst. Signal Process. 128 (2019) 497–530.
[9] F. Naets, J. Cuadrado, W. Desmet, Stable force identification in structural dynamics using Kalman filtering and dummy-measurements, Mech. Syst. Signal Process. 50 (2015) 235–248.
[10] M. Aucejo, O. De Smet, J. Deü, Practical issues on the applicability of Kalman filtering for reconstructing mechanical sources in structural dynamics, J. Sound Vib. 442 (2019) 45–70.
[11] T. Rogers, K. Worden, E. Cross, On the application of Gaussian process latent force models for joint input-state-parameter estimation: With a view to Bayesian operational identification, Mech. Syst. Signal Process. 140 (2020) 106580.
[12] R. Nayek, S. Narasimhan, Extraction of contact-point response in indirect bridge health monitoring using an input estimation approach, J. Civ. Struct. Health Monit. 10 (5) (2020) 815–831.
[13] J. Bietry, D. Delaunay, E. Conti, Comparison of full-scale measurement and computation of wind effects on a cable-stayed bridge, J. Wind Eng. Ind. Aerodyn. 57 (2–3) (1995) 225–235.
[14] J.H. Macdonald, Evaluation of buffeting predictions of a cable-stayed bridge from full-scale measurements, J. Wind Eng. Ind. Aerodyn. 91 (12–15) (2003) 1465–1483.
[15] Y. Xu, L. Zhu, Buffeting response of long-span cable-supported bridges under skew winds. Part 2: case study, J. Sound Vib. 281 (3–5) (2005) 675–697.
[16] L. Zhu, Y. Xu, Buffeting response of long-span cable-supported bridges under skew winds. Part 1: theory, J. Sound Vib. 281 (3–5) (2005) 647–673.
[17] H. Li, S. Laima, J. Ou, X. Zhao, W. Zhou, Y. Yu, N. Li, Z. Liu, Investigation of vortex-induced vibration of a suspension bridge with two separated steel box girders based on field measurements, Eng. Struct. 33 (6) (2011) 1894–1907.
[18] H. Li, S. Laima, Q. Zhang, N. Li, Z. Liu, Field monitoring and validation of vortex-induced vibrations of a long-span suspension bridge, J. Wind Eng. Ind. Aerodyn. 124 (2014) 54–67.
[19] A. Fenerci, O. Øiseth, Measured buffeting response of a long-span suspension bridge compared with numerical predictions based on design wind spectra, J. Struct. Eng. 143 (9) (2017) 04017131.
[20] F. Bastos, E. Caetano, A. Cunha, X. Cespedes, O. Flamand, Characterisation of the wind properties in the Grande Ravine viaduct, J. Wind Eng. Ind. Aerodyn. 173 (2018) 112–131.
[21] Y. Fujino, Vibration, control and monitoring of long-span bridges - recent research, developments and practice in Japan, J. Constr. Steel Res. 58 (1) (2002) 71–97.
[22] J. Ko, Y. Ni, Technology developments in structural health monitoring of large-scale bridges, Eng. Struct. 27 (12) (2005) 1715–1725.
[23] H.-N. Li, D.-S. Li, L. Ren, T.-H. Yi, Z.-G. Jia, L. Kun-Peng, Structural health monitoring of innovative civil engineering structures in Mainland China, Struct. Monit. Maint. 3 (1) (2016) 1.
[24] S. Bas, N.M. Apaydin, A. Ilki, F.N. Catbas, Structural health monitoring system of the long-span bridges in Turkey, Struct. Infrastruct. Eng. 14 (4) (2018) 425–444.
[25] A. Fenerci, K.A. Kvåle, Ø.W. Petersen, A. Rønnquist, O. Øiseth, Dataset for long-term wind and acceleration monitoring of the Hardanger Bridge, J. Struct. Eng. 147 (5) (2021) http://dx.doi.org/10.1061/(ASCE)ST.1943-541X.0002997.
[26] Ø.W. Petersen, O. Øiseth, E. Lourens, The use of inverse methods for response estimation of long-span suspension bridges with uncertain wind loading conditions, J. Civ. Struct. Health Monit. 9 (1) (2019) 21–36.
[27] Ø.W. Petersen, O. Øiseth, E. Lourens, Investigation of dynamic wind loads on a long-span suspension bridge identified from measured acceleration data, J. Wind Eng. Ind. Aerodyn. 196 (2020) http://dx.doi.org/10.1016/j.jweia.2019.104045.
[28] S. Zhang, T.J. Rogers, E.J. Cross, Gaussian process based grey-box modelling for SHM of structures under fluctuating environmental conditions, in: European Workshop on Structural Health Monitoring, Springer, 2020, pp. 55–66.
[29] A. Kareem, A. Tamura, Advanced Structural Wind Engineering, Springer, 2015.
[30] E. Strømmen, Theory of Bridge Aerodynamics, Springer Science & Business Media, 2010.
[31] E. Simiu, R.H. Scanlan, Wind Effects on Structures: Fundamentals and Applications to Design, John Wiley and Sons, 1996.
[32] R. Scanlan, N.P. Jones, A form of aerodynamic admittance for use in bridge aeroelastic analysis, J. Fluids Struct. 13 (7–8) (1999) 1017–1027.
[33] A.G. Davenport, The spectrum of horizontal gustiness near the ground in high winds, Q. J. R. Meteorol. Soc. 87 (372) (1961) 194–211.
[34] S. Krenk, Wind field coherence and dynamic wind forces, in: IUTAM Symposium on Advances in Nonlinear Stochastic Mechanics, Springer, 1996, pp. 269–278.
[35] T.M. Lystad, A. Fenerci, O. Øiseth, Buffeting response of long-span bridges considering uncertain turbulence parameters using the environmental contour method, Eng. Struct. 213 (2020) 110575.
[36] S. Särkkä, et al., Recursive Bayesian Inference on Stochastic Differential Equations, Helsinki University of Technology, 2006.
[37] C.E. Rasmussen, Gaussian Processes in Machine Learning, MIT Press, 2006, pp. 63–71.
[38] M. Alvarez, D. Luengo, N.D. Lawrence, Latent force models, in: Artificial Intelligence and Statistics, 2009, pp. 9–16.
[39] J. Hartikainen, S. Särkkä, Kalman filtering and smoothing solutions to temporal Gaussian process regression models, in: 2010 IEEE International Workshop on Machine Learning for Signal Processing, IEEE, 2010, pp. 379–384.
[40] A. Solin, S. Särkkä, Explicit link between periodic covariance functions and state space models, in: Artificial Intelligence and Statistics, PMLR, 2014, pp. 904–912.
[41] S. Reece, S. Roberts, S. Ghosh, A. Rogers, N.R. Jennings, Efficient state-space inference of periodic latent force models, J. Mach. Learn. Res. 15 (2014) 2337–2397.

[42] A. Grigorievskiy, J. Karhunen, Gaussian process kernels for popular state-space time series models, in: 2016 International Joint Conference on Neural Networks (IJCNN), IEEE, 2016, pp. 3354–3363.
[43] A. Solin, S. Särkkä, Gaussian quadratures for state space approximation of scale mixtures of squared exponential covariance functions, in: 2014 IEEE International Workshop on Machine Learning for Signal Processing (MLSP), IEEE, 2014, pp. 1–6.
[44] T. Karvonen, S. Sarkkä, Approximate state-space Gaussian processes via spectral transformation, in: 2016 IEEE 26th International Workshop on Machine Learning for Signal Processing (MLSP), IEEE, 2016, pp. 1–6.
[45] R.E. Kalman, A new approach to linear filtering and prediction problems, J. Basic Eng. 82 (1) (1960) 35–45.
[46] H.E. Rauch, F. Tung, C.T. Striebel, Maximum likelihood estimates of linear dynamic systems, AIAA J. 3 (8) (1965) 1445–1450.
[47] A. Fenerci, O. Øiseth, A. Rønnquist, Long-term monitoring of wind field characteristics and dynamic response of a long-span suspension bridge in complex terrain, Eng. Struct. 147 (2017) 269–284.
[48] J.C. Kaimal, J. Wyngaard, Y. Izumi, O. Coté, Spectral characteristics of surface-layer turbulence, Q. J. R. Meteorol. Soc. 98 (417) (1972) 563–589.
[49] J. Mann, L. Kristensen, N. Jensen, Uncertainties of extreme winds, spectra, and coherences, in: International Symposium on Advances in Bridge Aerodynamics, CRC Press/Balkema, 1998, pp. 49–56.
[50] L. Kristensen, N. Jensen, Lateral coherence in isotropic turbulence and in the natural wind, Bound.-Lay. Meteorol. 17 (3) (1979) 353–373.
[51] Ø.W. Petersen, O. Øiseth, Finite element model updating of a long span suspension bridge, in: R. Rupakhety, S. Olafsson, B. Bessason (Eds.), Proceedings of the International Conference on Earthquake Engineering and Structural Dynamics, Springer International Publishing, 2019, pp. 335–344.
[52] O. Øiseth, A. Rönnquist, R. Sigbjörnsson, Simplified prediction of wind-induced response and stability limit of slender long-span suspension bridges, based on modified quasi-steady theory: a case study, J. Wind Eng. Ind. Aerodyn. 98 (12) (2010) 730–741.
[53] B. Siedziako, O. Øiseth, A. Rønnquist, An enhanced forced vibration rig for wind tunnel testing of bridge deck section models in arbitrary motion, J. Wind Eng. Ind. Aerodyn. 164 (2017) 152–163.
[54] M. Döhler, L. Mevel, Efficient multi-order uncertainty computation for stochastic subspace identification, Mech. Syst. Signal Process. 38 (2) (2013) 346–366.
[55] E. Reynders, R. Pintelon, G. De Roeck, Uncertainty bounds on modal parameters obtained from stochastic subspace identification, Mech. Syst. Signal Process. 22 (4) (2008) 948–969.
[56] S. Särkkä, Bayesian Filtering and Smoothing, Vol. 3, Cambridge University Press, 2013.
[57] H. Zhang, Inconsistent estimation and asymptotically equal interpolations in model-based geostatistics, J. Amer. Statist. Assoc. 99 (465) (2004) 250–261.
[58] Z. Ying, Asymptotic properties of a maximum likelihood estimator with data from a Gaussian process, J. Multivariate Anal. 36 (2) (1991) 280–296.
[59] Ø.W. Petersen, G.T. Frøseth, O. Øiseth, Design and deployment of a monitoring system on a long-span suspension bridge, in: 10th International Conference on Structural Health Monitoring of Intelligent Infrastructure, SHMII 2021, 2021.
[60] B.D.O. Anderson, M. John B. Moore, Optimal Filtering, Prentice-Hall, New Jersey, USA, 1979.
[61] F.L. Lewis, L. Xie, D. Popa, Optimal and Robust Estimation: With an Introduction to Stochastic Control Theory, second ed., Taylor & Francis Group, Florida, USA, 2007.
[62] D. Simon, Optimal State Estimation: Kalman, H Infinity, and Nonlinear Approaches, John Wiley & Sons, 2006.
[63] W.W.S. Wei, Time Series Analysis: Univariate and Multivariate Methods, Pearson, 2006.
[64] Y. Tingyan, Multistep Yule-Walker Estimation of a Autoregressive Models (Master's thesis), National University of Singapore, 2010.